the CENP-A nucleosome, resulting in higher reconstitution efficiencies on a 147-base-pair DNA.

A superimposition of CENP-A and H3 reveals a clear difference in the loop 1 region (residues Phe 78–Phe 84 of CENP-A), where CENP-A has two extra amino acid residues (Arg 80 and Gly 81) compared to H3 (Fig. 2a). The CENP-A loop 1 protrudes from the CENP-A nucleosome, and the Arg 80 and Gly 81 residues are located at the tip of the loop (Fig. 3 and Supplementary Fig. 11). In the free CENP-A–H4 tetramer structure, the loop 1 region is more flexible than the other CENP-A regions, as judged from the B-factors. By contrast, in the CENP-A nucleosome, the B-factors of the loop 1 region are similar to those of the other regions (Supplementary Fig. 12), indicating that CENP-A nucleosome formation may stabilize the loop 1 region. The tip of the loop 1 region is solvent-accessible (Fig. 3), and may function as a binding site for *trans*-acting factors that interact directly with the CENP-A nucleosome. To test the functional significance of the CENP-A Arg 80 and Gly 81 residues, we co-expressed the green fluorescent protein (GFP)-tagged CENP-A and the red fluorescent protein (RFP)-tagged CENP-A(del), in which the Arg 80 and Gly 81 residues were deleted, in human-telomerase-immortalized retina pigment epithelial (hTERT-RPE1) cells. Within 1 or 2 days after transfection, both GFP-tagged CENP-A and RFP-tagged CENP-A(del) were recruited to the centromeres, which were identified by a constitutive centromere protein, CENP-C (Fig. 4a). This result indicates that the Arg 80 and Gly 81 residues are not essential for targeting CENP-A to the centromeres. However, 3 days after transfection, the number of cells in which the CENP-A(del) signals were detected at the centromeres was markedly reduced (Fig. 4b). Concomitantly, the number of cells with the CENP-A signal alone increased (Fig. 4b). Similar results were obtained when the fluorescent labels were swapped between CENP-A and CENP-A(del), showing that the phenomenon does not depend on the fusion partner (Fig. 4c). These results indicate that CENP-A(del) is less stably incorporated into centromeres, compared to CENP-A. In addition, two CENP-A mutants, one containing the Arg 80-Gly 81 to Ala 80-Ala 81 substitution (CENP-A(A80A81)) and another with the Val 82-Asp 83 deletion, which disrupts the Arg 80-Gly 81 protrusion (CENP-A(del82-83)), were targeted to centromeres at levels comparable to those of CENP-A, 1 day after transfection. The number of cells retaining the CENP-A mutants at the centromeres also decreased, 3 days after transfection (Supplementary Fig. 13a, b). However, like CENP-A, the CENP-A mutant containing the Val 82-Asp 83 to Ala82-Ala83 substitution (CENP-A(A82A83)) remained at the centromeres, 3 days after transfection (Supplementary Fig. 13c). Thus, the Arg 80 and Gly 81 residues and the size of the protruding loop 1 are critical for stable CENP-A retention at centromeres.

There has been much debate over the CENP-A nucleosome structure and its role in the centromere-specific chromatin structure. Because CENP-A has lower sequence homology to H3, compared to

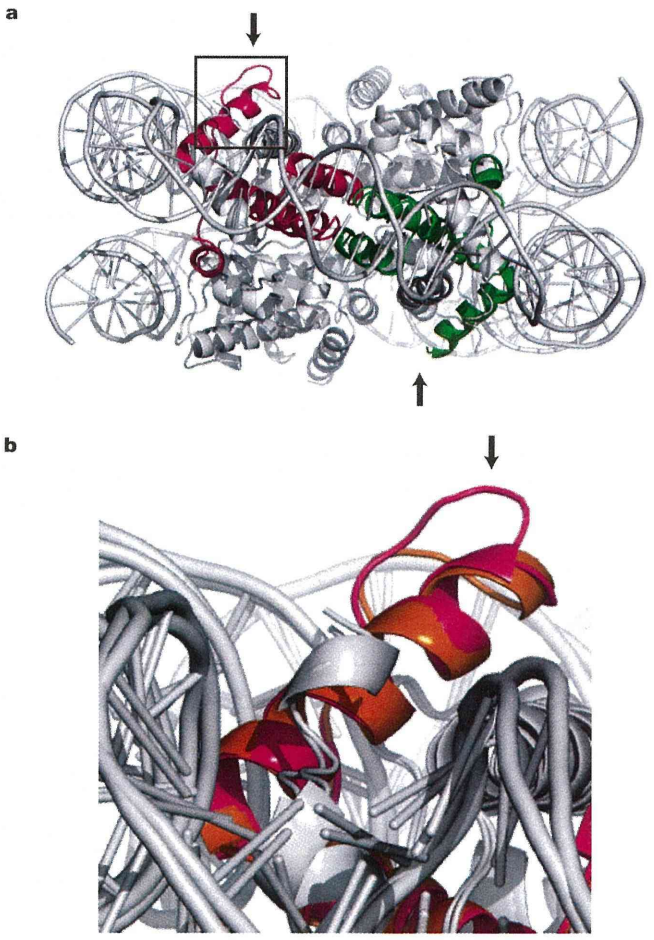

Figure 3 | Structural differences in the loop 1 regions between CENP-A and H3. **a**, Side view of the CENP-A nucleosome. The CENP-A molecules are shown in magenta and green. The box indicates the region enlarged in panel **b**. **b**, Superimposition of the CENP-A (magenta) and H3 (orange) loop 1 regions. Arrows indicate the tip of the CENP-A loop 1 containing the Arg 80 and Gly 81 residues.

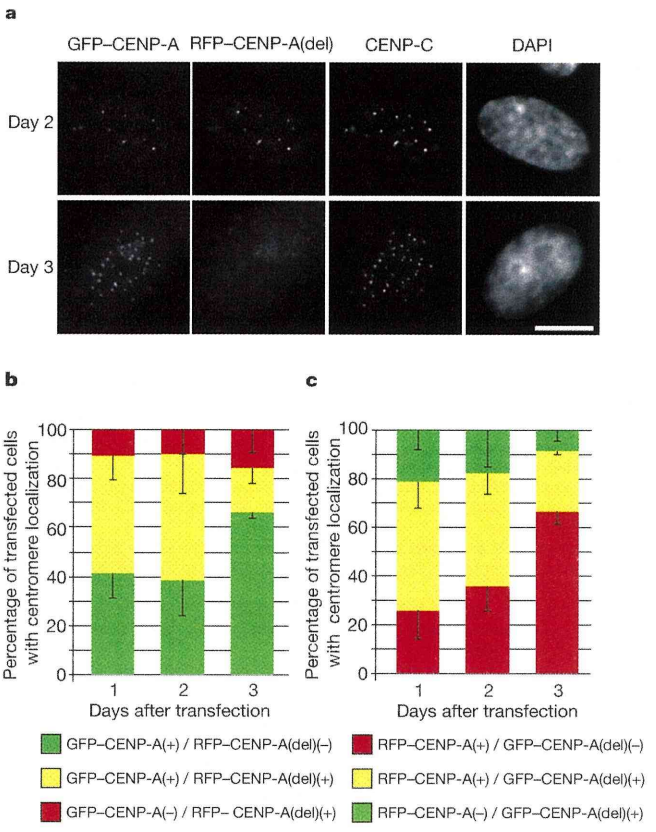

Figure 4 | Less stable association of CENP-A(del) with the centromere. **a**, Fluorescence images. hTERT-RPE1 cells were transfected with GFP-tagged CENP-A and RFP-tagged CENP-A(del), fixed, and stained with anti-CENP-C (Cy5) and DAPI. Bar, 10 μm. **b**, Quantitative data. Using images such as those in panel **a**, the numbers of transfected hTERT-RPE1 cells showing GFP–CENP-A, RFP–CENP-A(del), or both at centromeres were counted ($n > 28$), and the average percentages from three independent transfections were plotted with the standard deviations. **c**, hTERT-RPE1 cells were transfected with GFP-tagged CENP-A(del) and RFP-tagged CENP-A, and were analysed as described in panel **b** ($n > 20$).

©2011 Macmillan Publishers Limited. All rights reserved

other H3 variants, the possibility of a CENP-A nucleosome composed of one of each core histone (hemisome) is an attractive proposition. However, our findings support the octasome model for the CENP-A nucleosome. It is still possible that both types of CENP-A nucleosomes, octasome and hemisome, coexist in the functional centromeric chromatin *in vivo*. We also cannot exclude the possibility that CENP-A hemisomes can be reconstituted under different conditions and/or with factor(s) required for their assembly. Nevertheless, the present structure suggests that the fundamental principles involved in nucleosome formation are likely to be similar among the H3 variants, including CENP-A. The flexibility exclusively observed in the DNA regions located at the entrance and the exit of the CENP-A nucleosome and the loop 1 region protruding from the CENP-A nucleosome may have an essential role in the centromeric chromatin architecture.

METHODS SUMMARY

Human CENP-A, H2A, H2B, H3.1 and H4 were overexpressed in *Escherichia coli* cells, and were purified by a method described previously[21,23–25]. Details are provided in Methods. The 147-base-pair DNA used in the CENP-A nucleosome reconstitution was prepared by self-ligation with the 71-base-pair fragment of a human α-satellite sequence[16,21], containing an extra 5-base overhang, 5′-GTAAC-3′, for the cohesive end. The resultant 147-base-pair DNA contained the CENP-B box near both edges, and an A:A mismatch was located at the centre of the DNA (Supplementary Fig. 2). The preparation, crystallization and structural determination of the CENP-A nucleosome are described in Methods. Analyses of the fluorescent protein-tagged CENP-A or CENP-A mutant incorporation at centromeres were performed using hTERT-RPE1 cells. Details are described in Methods.

Full Methods and any associated references are available in the online version of the paper at www.nature.com/nature.

Received 29 August 2010; accepted 1 June 2011.
Published online 10 July 2011.

1. Cheeseman, I. M. & Desai, A. Molecular architecture of the kinetochore-microtubule interface. *Nature Rev. Mol. Cell Biol.* **9,** 33–46 (2008).
2. Santaguida, S. & Musacchio, A. The life and miracles of kinetocores. *EMBO J.* **28,** 2511–2531 (2009).
3. Palmer, D. K., O'Day, K., Wener, M. H., Andrews, B. S. & Margolis, R. L. A 17-kD centromere protein (CENP-A) copurifies with nucleosome core particles and with histones. *J. Cell Biol.* **104,** 805–815 (1987).
4. Stoler, S., Keith, K. C., Curnick, K. E. & Fitzgerald-Hayes, M. A mutation in CSE4, an essential gene encoding a novel chromatin-associated protein in yeast, causes chromosome nondisjunction and cell cycle arrest at mitosis. *Genes Dev.* **9,** 573–586 (1995).
5. Meluh, P. B., Yang, P., Glowczewski, L., Koshland, D. & Smith, M. M. Cse4p is a component of the core centromere of *Saccharomyces cerevisiae*. *Cell* **94,** 607–613 (1998).
6. Buchwitz, B. J., Ahmad, K., Moore, L. L., Roth, M. B. & Henikoff, S. A histone-H3-like protein in *C. elegans*. *Nature* **401,** 547–548 (1999).
7. Henikoff, S., Ahmad, K., Platero, J. S. & van Steensel, B. Heterochromatic deposition of centromeric histone H3-like proteins. *Proc. Natl Acad. Sci. USA* **97,** 716–721 (2000).
8. Howman, E. V. *et al.* Early disruption of centromeric chromatin organization in centromere protein A (*Cenpa*) null mice. *Proc. Natl Acad. Sci. USA* **97,** 1148–1153 (2000).
9. Takahashi, K., Chen, E. S. & Yanagida, M. Requirement of Mis6 centromere connector for localizing a CENP-A-like protein in fission yeast. *Science* **288,** 2215–2219 (2000).
10. Blower, M. D. & Karpen, G. H. The role of *Drosophila* CID in kinetochore formation, cell-cycle progression and heterochromatin interactions. *Nature Cell Biol.* **3,** 730–739 (2001).
11. Oegema, K., Desai, A., Rybina, S., Kirkham, M. & Hyman, A. A. Functional analysis of kinetochore assembly in *Caenorhabditis elegans*. *J. Cell Biol.* **153,** 1209–1226 (2001).
12. Régnier, V. *et al.* CENP-A is required for accurate chromosome segregation and sustained kinetochore association of BubR1. *Mol. Cell. Biol.* **25,** 3967–3981 (2005).
13. Luger, K., Mäder, A. W., Richmond, R. K., Sargent, D. F. & Richmond, T. J. Crystal structure of the nucleosome core particle at 2.8 Å resolution. *Nature* **389,** 251–260 (1997).
14. Talbert, P. B. & Henikoff, S. Histone variants—ancient wrap artists of the epigenome. *Nature Rev. Mol. Cell Biol.* **11,** 264–275 (2010).
15. Yoda, K. *et al.* Human centromere protein A (CENP-A) can replace histone H3 in nucleosome reconstitution *in vitro*. *Proc. Natl Acad. Sci. USA* **97,** 7266–7271 (2000).
16. Tanaka, Y. *et al.* Human centromere protein B induces translational positioning of nucleosomes on alpha-satellite sequences. *J. Biol. Chem.* **280,** 41609–41618 (2005).
17. Camahort, R. *et al.* Cse4 is part of an octameric nucleosome in budding yeast. *Mol. Cell* **35,** 794–805 (2009).
18. Dalal, Y., Wang, H., Lindsay, S. & Henikoff, S. Tetrameric structure of centromeric nucleosomes in interphase *Drosophila* cells. *PLoS Biol.* **5,** e218 (2007).
19. Dalal, Y., Furuyama, T., Vermaak, D. & Henikoff, S. Structure, dynamics, and evolution of centromeric nucleosomes. *Proc. Natl Acad. Sci. USA* **104,** 15974–15981 (2007).
20. Furuyama, T. & Henikoff, S. Centromeric nucleosomes induce positive DNA supercoils. *Cell* **138,** 104–113 (2009).
21. Tanaka, Y. *et al.* Expression and purification of recombinant human histones. *Methods* **33,** 3–11 (2004).
22. Tsunaka, Y., Kajimura, N., Tate, S. & Morikawa, K. Alteration of the nucleosomal DNA path in the crystal structure of a human nucleosome core particle. *Nucleic Acids Res.* **33,** 3424–3434 (2005).
23. Tachiwana, H. *et al.* Structural basis of instability of the nucleosome containing a testis-specific histone variant, human H3T. *Proc. Natl Acad. Sci. USA* **107,** 10454–10459 (2010).
24. Tachiwana, H., Osakabe, A., Kimura, H. & Kurumizaka, H. Nucleosome formation with the testis-specific histone H3 variant, H3t, by human nucleosome assembly proteins *in vitro*. *Nucleic Acids Res.* **36,** 2208–2218 (2008).
25. Osakabe, A. *et al.* Nucleosome formation activity of human somatic nuclear autoantigenic sperm protein (sNASP). *J. Biol. Chem.* **285,** 11913–11921 (2010).
26. Sekulic, N., Bassett, E. A., Rogers, D. J. & Black, B. E. The structure of $(CENP\text{-}A\text{–}H4)_2$ reveals physical features that mark centromeres. *Nature* **467,** 347–351 (2010).
27. Conde e Silva, N. *et al.* CENP-A-containing nucleosomes: easier disassembly versus exclusive centromeric localization. *J. Mol. Biol.* **370,** 555–573 (2007).
28. Kingston, I. J., Yung, J. S. & Singleton, M. R. Biophysical characterisation of the centromere-specific nucleosome from budding yeast. *J. Biol. Chem.* **286,** 4021–4026 (2011).
29. Schalch, T., Duda, S., Sargent, D. F. & Richmond, T. J. X-ray structure of a tetranucleosome and its implications for the chromatin fibre. *Nature* **436,** 138–141 (2005).
30. Masumoto, H., Masukata, H., Muro, Y., Nozaki, N. & Okazaki, T. A human centromere antigen (CENP-B) interacts with a short specific sequence in alphoid DNA, a human centromeric satellite. *J. Cell Biol.* **109,** 1963–1973 (1989).

Supplementary Information is linked to the online version of the paper at www.nature.com/nature.

Acknowledgements We thank the beamline scientists, N. Shimizu, Y. Kawano, M. Makino and T. Hikima, for their assistance with data collection at the BL41XU and BL45XU beamlines of SPring-8. We also thank R. Matsumoto for technical assistance, K. Yoda for anti-CENP-C, and T. Fukagawa and Y. Hiraoka for discussions. This work was supported in part by Grants-in-Aid from the Japanese Society for the Promotion of Science (JSPS), and the Ministry of Education, Culture, Sports, Science and Technology (MEXT), Japan. H.Ku. was also supported by the Waseda Research Institute for Science and Engineering.

Author Contributions H.T., T.S., A.O. and Y.M. purified the histones and CENP-A, crystallized the CENP-A nucleosome, and performed biochemical analyses. H.T., W.K., K.S. and T.S. collected X-ray diffraction data, and H.T., W.K., and S.-Y.P. performed the structural analysis of the CENP-A nucleosome. H.T., A.O., Y.H.-T. and H.Ki. performed the cell biological experiments. T.O., H.T., W.K. and M.S. performed SAXS analysis. H.Ku. conceived, designed and supervised all of the work, and H.Ku., W.K. and H.T. wrote the paper. All of the authors discussed the results and commented on the manuscript.

Author Information The atomic coordinates of the CENP-A nucleosome have been deposited in the Protein Data Bank, under the accession code 3AN2. Reprints and permissions information is available at www.nature.com/reprints. The authors declare no competing financial interests. Readers are welcome to comment on the online version of this article at www.nature.com/nature. Correspondence and requests for materials should be addressed to H.Ku. (kurumizaka@waseda.jp).

©2011 Macmillan Publishers Limited. All rights reserved

METHODS

Overexpression of human histones. Human histones H2A and H2B were produced in *Escherichia coli* BL21(DE3) cells, and histone H4 was produced in *E. coli* JM109(DE3) cells. Human CENP-A was produced in *E. coli* DH5α cells. All histones and CENP-A were produced in *E. coli* cells in the absence of T7 RNA polymerase by omitting the addition of isopropyl-β-D-thiogalactopyranoside, which induces the T7 RNA polymerase production in BL21(DE3) and JM109(DE3) cells. All histones and CENP-A were produced as N-terminal His_6-tagged proteins, as described previously[21]. The His_6 tags of all histones were removed by thrombin protease digestion, leaving a Gly-Ser-His sequence at the N-terminal end of each histone.

For the purpose of structural determination, selenomethionine (Se-Met)-substituted H2B was produced in *E. coli* B834(DE3) cells, using the pET15b vector system (Novagen). The B834(DE3) cells were grown in 100 ml of LB medium for 4 h at 37 °C. The cells were collected and transferred into 300 ml of M9 medium (+50 μg ml^{-1} Se-Met). After 12 h growth at 37 °C, the 300-ml culture was added to 2 l of M9 medium (+50 μg ml^{-1} Se-Met), and the culture was continued at 37 °C. When the cell density reached 0.5 (D_{600}), isopropyl-β-D-thiogalactopyranoside (final concentration 1 mM) was added, to induce the expression of H2B. The cells were grown further at 37 °C for 12 h.

Purification of human histones. The cells producing recombinant histones were collected, and were resuspended in 50 ml of buffer A (50 mM Tris-HCl (pH 8.0), 500 mM NaCl, 1 mM PMSF and 5% glycerol). The cells were disrupted by two rounds of sonication for 200 s each. The cell lysates were centrifuged at 27,216*g* for 20 min at 4 °C. The supernatants were discarded, and the pellet containing the His_6-tagged histones was resuspended in 50 ml of buffer A, containing 7 M guanidine hydrochloride. The samples were rotated for 12 h at 4 °C, and the supernatants were recovered by centrifugation at 27,216*g* for 20 min at 4 °C. The supernatants containing the His_6-tagged histones were combined with 4 ml (50% slurry) of nickel-nitrilotriacetic acid (Ni-NTA) agarose resin (Qiagen), and the samples were rotated for 1 h at 4 °C. The agarose beads were then washed with 100 ml of buffer B (50 mM Tris-HCl (pH 8.0), 500 mM NaCl, 6 M urea, 5 mM imidazole, and 5% glycerol). The His_6-tagged histones were eluted by a 100-ml linear gradient of 5 to 500 mM imidazole in buffer B, and the samples were dialysed against buffer C (5 mM Tris-HCl (pH 7.5) and 2 mM 2-mercaptoethanol). The N-terminal His_6 tags were removed from the histones by thrombin protease treatment (1 unit mg^{-1} of histones; GE Healthcare) at room temperature for 3 h. The removal of the His_6 tags was confirmed by SDS–16% polyacrylamide gel electrophoresis (PAGE); the recombinant histones without the His_6 tag migrated faster than the His_6-tagged histones. After the His_6 tag was uncoupled, each histone was subjected to Mono S column chromatography (GE Healthcare). The column was washed with buffer D (20 mM sodium acetate (pH 5.2), 200 mM NaCl, 5 mM 2-mercaptoethanol, 1 mM EDTA, and 6 M urea), and each histone was eluted by a linear gradient of 200 to 800 mM NaCl in buffer D. The purified histones were dialysed against water, and were freeze-dried.

Preparation of DNAs. The 147-base-pair DNA, which was used for reconstituting the CENP-A nucleosome, is a derivative of the human α-satellite DNA (sat4)[21]. The EcoRI site (GAATTC) of the sat4 sequence was replaced by a BstPI site (GGTAACC). The 71-mer DNA fragment containing the 5′ half of the sat4 sequence, with the CENP-B box at the edge, was ligated in tandem in the plasmid (p5′Sat4-24). The 71-mer DNA fragment containing an extra 5-base overhang, 5′-GTAAC-3′, was prepared for self-ligation according to the method described previously[31]. The 71-mer DNA fragment containing the 5-base overhang was self-ligated, and the palindromic 147-base-pair α-satellite DNA derivative was prepared. The 147-base-pair DNA sequence is: 5′-ATCCTTCGTTGGAAACG GGATTTCTTCATTTCATGCTAGACAGAAGAATTCTCAGTAACTTCTTTG TGCTGGTAACCAGCACAAAGAAGTTACTGAGAATTCTTCTGTCTAGCAT GAAATGAAGAAATCCCGTTTCCAACGAAGGAT-3′.

In this palindromic 147-base-pair α-satellite DNA derivative, an A:A mismatch was introduced at the centre of the 147-base-pair DNA fragment (underlined).

Preparation of the CENP-A nucleosome. The purified H2A–H2B (Se-Met)–CENP-A–H4 (0.9 mg) and the 147-base-pair DNA (1 mg) were mixed in a solution containing 2 M KCl, and the sample was dialysed against dialysis buffer (10 mM Tris-HCl (pH 7.5), 1 mM EDTA, 1 mM dithiothreitol and 2 M KCl). After dialysis at 4 °C for 3 h, the KCl concentration of the dialysis buffer was gradually decreased to 250 mM with a peristaltic pump (0.8 ml min^{-1} flow rate). The sample was then dialysed against 10 mM Tris-HCl buffer (pH 7.5), containing 1 mM EDTA, 1 mM dithiothreitol and 250 mM KCl, at 4 °C for 3 h. After this dialysis step, the sample was incubated at 55 °C for 2 h. The CENP-A nucleosome was purified from the free DNA and histones by non-denaturing polyacrylamide gel electrophoresis, using a Prep Cell apparatus (Bio-Rad). The purified CENP-A nucleosome was concentrated, and was dialysed against 20 mM potassium cacodylate buffer (pH 6.0) containing 1 mM EDTA.

Crystallization and structure determination. Crystals of the purified CENP-A nucleosome were obtained by the hanging drop method, after mixing equal volumes of the CENP-A nucleosome solution and 20 mM potassium cacodylate buffer (pH 6.0), containing 60–96 mM KCl and 135–144 mM $MnCl_2$. The CENP-A nucleosome sample was equilibrated against a reservoir solution of 20 mM potassium cacodylate (pH 6.0), 38–56 mM KCl, and 70–75 mM $MnCl_2$. Crystals of the CENP-A nucleosome were soaked in a cryoprotectant solution, containing 20 mM potassium cacodylate (pH 6.0), 47 mM KCl, 72 mM $MnCl_2$, 30% polyethylene glycol 400, and 5% trehalose. The crystals were flash-cooled in a stream of N_2 gas (100 K). The CENP-A nucleosome crystals belonged to the monoclinic space group $P2_1$, with unit cell constants of $a = 65.8$ Å, $b = 83.3$ Å, $c = 176.8$ Å and $\beta = 100.7°$, and contained one nucleosome in the asymmetric unit. High-resolution diffraction data were obtained using the synchrotron radiation source at the beamline BL41XU station of SPring-8, Harima, Japan.

Diffraction data of the CENP-A nucleosome were integrated and scaled with the HKL2000 program[32]. The data were processed with the CCP4 program suite[33]. The structure was solved by the molecular replacement method, using the MOLREP program[34] and the human nucleosome structure (PDB accession number 3AFA) as a search model[23]. Most of the amino acid side chains were clearly visible in the map initially calculated at 3.6 Å resolution. Rigid body refinement of the obtained solution was performed using the CNS program[35]. Further structural refinement consisted of iterative rounds of energy minimization and B factor refinement using the CNS program[35], and model building using the COOT program[36]. The Ramachandran plot of the final structure showed 98.7% of the residues in the most favourable and additional allowed regions, and no residues in the disallowed region. Summaries of the data collection and refinement statistics are provided in Supplementary Table 1. All structure figures were created using the PyMOL program (http://pymol.org). The atomic coordinates of the CENP-A nucleosome have been deposited in the Protein Data Bank, with the ID code 3AN2.

Supercoiling assay. Salt-dialysis supercoiling assay. Relaxed plasmid DNA (500 ng) was mixed with 0, 125, 250, 500 and 1,000 ng of histone octamer in 5 μl of 20 mM Tris-HCl (pH 7.5) buffer, containing 1 mM EDTA, 0.2 mg ml^{-1} BSA, and 2 M NaCl. The samples were then incubated at 37 °C for 30 min. The NaCl concentration of the sample was reduced to 1 M, 0.8 M, 0.67 M, and 0.2 M by adding dilution buffer, containing 20 mM Tris-HCl (pH 7.5), 1 mM EDTA, 0.2 mg ml^{-1} BSA, 5 mM $MgCl_2$, and 0.06 U μl^{-1} calf (Invitrogen) or wheat germ (Promega) topoisomerase I. The samples were incubated at 37 °C for 30 min in each dilution step.

Chaperone-mediated supercoiling assay. NAP1 or sNASP (0.25, 0.5, and 1.0 μM) was pre-incubated with H2A–H2B (150 ng) and CENP-A–H4 (150 ng) at 37 °C for 15 min. Supercoiled plasmid DNA (100 ng), which was relaxed with a topoisomerase I solution (10 mM Tris-HCl (pH 8.0), 2 mM $MgCl_2$, 5 mM dithiothreitol, and 2 U μl^{-1} wheat germ topoisomerase I (Promega)), was added to the reaction mixture. The samples were then incubated at 37 °C for 60 min in 10 mM Tris-HCl (pH 8.0) buffer, containing 140 mM NaCl, 2 mM $MgCl_2$, and 5 mM dithiothreitol, followed by an incubation at 42 °C for 60 min.

In both the salt-dialysis and chaperone-mediated assays, after the reaction, the samples were treated with 50 μl of a proteinase K solution (20 mM Tris-HCl (pH 8.0), 20 mM EDTA, 0.5% SDS, and 0.5 mg ml^{-1} proteinase K (Roche)) at 37 °C for 30 min. The DNA was extracted with phenol/chloroform. The DNA was then precipitated by ethanol, and was analysed by one-dimensional gel electrophoresis on a 1% agarose gel in 1 × TAE buffer (for the salt-dialysis assay, 1.3 V cm^{-1} for 15.5 h) or 1× TBE buffer (for the chaperone-mediated assay, 1.3 V cm^{-1} for 15.5 h). For the two-dimensional gel electrophoresis, the DNA was electrophoresed on a 0.7% agarose gel in 1× TBE buffer (for the salt-dialysis assay, 2 V cm^{-1} for 7 h) or a 1% agarose gel in 1× TBE buffer (for the chaperone-mediated assay, 1.3 V cm^{-1} for 15 h) for the first dimension. The gel was then soaked in 1× TBE buffer containing 4 mg l^{-1} of chloroquine for 3 h. The samples were subsequently electrophoresed in 1× TBE buffer containing 4 mg l^{-1} of chloroquine (1.3 V cm^{-1} for 12 h (for the salt-dialysis assay) or 1.3 V cm^{-1} for 15 h (for the chaperone-mediated assay)) for the second dimension. The DNA was visualized by SYBR Gold (Invitrogen) staining.

Nucleosome reconstitution by the salt-dialysis method for biochemical analyses. The purified H2A–H2B–CENP-A–H4 or H2A–H2B–H3–H4 octamer was mixed with a DNA fragment (300 μg, 121-base-pair DNA or 147-base-pair DNA) in a solution containing 2 M KCl (376 μl). The amounts of histone octamers were 420 μg for the 121-base-pair DNA and 384 μg for the 147-base-pair DNA. Nucleosomes were reconstituted and prepared by the same method as described in the 'Preparation of the CENP-A nucleosome' section.

Competitive nucleosome assembly assay. The purified H2A–H2B–CENP-A–H4 octamer (14, 28, 42 or 56 μg) was incubated in the presence of both the 147-base-pair DNA (24 μg) and 121-base-pair DNA (20 μg), in a solution containing 2 M KCl, and the sample was dialysed against dialysis buffer (10 mM Tris-HCl

©2011 Macmillan Publishers Limited. All rights reserved

(pH 7.5), 1 mM EDTA, 1 mM dithiothreitol, and 2 M KCl). After dialysis at 4 °C for 3 h, the KCl concentration of the dialysis buffer was gradually decreased to 250 mM with a peristaltic pump (0.8 ml min^{-1} flow rate). The sample was then dialysed against 10 mM Tris-HCl buffer (pH 7.5), containing 1 mM EDTA, 1 mM dithiothreitol, and 250 mM KCl, at 4 °C for 3 h. The CENP-A nucleosomes were then analysed by 6% PAGE in 0.2× TBE buffer (18 mM Tris base, 18 mM boric acid, and 0.4 mM EDTA) at 16 V cm^{-1} for 1 h, followed by ethidium bromide staining.

Nucleosome disruption assay. The CENP-A nucleosomes were reconstituted with a 121-base-pair or 147-base-pair palindromic α-satellite derivative, by the salt dialysis method. The 121-base-pair DNA lacks the 13-base-pair regions from both edges of the 147-base-pair DNA used in the crystallography of the CENP-A nucleosome. The rest of the 121-base-pair DNA sequence is identical to the 147-base-pair palindromic α-satellite derivative. The CENP-A nucleosomes (150 ng) were incubated at 37 °C, 57 °C, 67 °C, 70 °C, or 73 °C for 15 min in the presence of supercoiled plasmid DNA (100 ng). After the incubation, the CENP-A nucleosomes that were not disrupted were separated by non-denaturing 6% PAGE, and were visualized by ethidium bromide staining. The relative band intensities for the CENP-A nucleosomes were quantified and plotted against the temperature.

Exonuclease assay. The reconstituted CENP-A or H3 nucleosomes were treated with 3 units of *Escherichia coli* exonuclease III (Takara), in 10 μl of 50 mM Tris-HCl (pH 8.0), 5 mM $MgCl_2$, and 1 mM DTT. After an incubation for 0, 2, 4, or 8 min at 37 °C, the reaction was stopped by the addition of 55 μl of proteinase K solution (20 mM Tris-HCl (pH 8.0), 20 mM EDTA, 0.5% SDS, and 0.5 mg ml^{-1} proteinase K (Roche)). After a 15 min incubation at room temperature, the DNA was extracted with phenol/chloroform, precipitated with ethanol, dissolved in Hi-Di Formamide (Applied Biosystems), and then analysed by 10% denaturing PAGE with a gel containing 7 M urea in 0.5× TBE buffer (21 V cm^{-1} for 1.5 h).

Small-angle X-ray scattering (SAXS). SAXS measurements of the reconstituted CENP-A and H3 nucleosomes, in 20 mM Tris-HCl buffer (pH 7.5) containing 1 mM EDTA and 1 mM DTT, were performed at the RIKEN structural biology beam-line I (BL45XU) of SPring-8 (Hyogo, Japan)[37]. Scattering intensities of the nucleosome solutions were measured with an R-AXIS IV^{++} imaging plate detector at 20 °C with a sample-to-detector distance of 3,529 mm, which was calibrated by the powder diffraction from silver docosanoate. Circular averaging of the scattering intensities was then performed to obtain the one-dimensional scattering data $I(q)$ as a function of q ($q = 4\pi\sin\theta/\lambda$), where 2θ is the scattering angle and the X-ray wavelength $\lambda = 0.9$ Å). Three successive measurements were made for each solution, with an exposure time of 60 s. The resultant three data sets were combined after inspections for X-ray radiation damage to the solution and the existence of instrumental artefacts. SAXS measurements of the buffer solution for background subtraction were performed after each measurement of the nucleosome solutions, using the same conditions and procedure as those of the nucleosome solutions. To correct the inter-particle interference effect, $I(q)$ data were collected at four protein concentrations (0.5, 0.7, 1.0 and 1.3 mg ml^{-1}), and extrapolated to zero concentration. The data were processed and analysed using the software applications embedded in the ATSAS package (http://www.embl-hamburg.de/biosaxs/software.html). The radius of gyration, R_g, was estimated by fitting the $I(q)$ data using the Guinier approximation $I(q) = I(0)\exp(-q^2R_g^2/3)$, where $I(0)$ is the forward scattering at the zero scattering angle, in a smaller angle region of $qR_g < 1.3$. Error of R_g was estimated from the least-squares fitting. The distance distribution function $P(r)$ and its error were calculated by the program GNOM[38]. The maximum dimension D_{max} was estimated from the $P(r)$ function as the distance r, where $P(r) = 0$ (ref. 39), and its error was estimated from the errors of the $P(r)$ values around $P(r) = 0$.

Centromere localization of CENP-A and CENP-A mutants. hTERT-RPE1 cells were transfected with combinations of wild-type CENP-A and CENP-A(del), in which two amino acid residues (the Arg 80 and Gly 81 residues of the CENP-A loop 1) were deleted, and tagged with either GFP or RFP, using GeneJuice (Merck) according to the manufacturer's instructions. hTERT-RPE1 cells were also transfected with combinations of wild-type CENP-A tagged with RFP and CENP-A(del82-83) (where the Val 82 and Asp 83 residues of the CENP-A loop 1 were deleted), or CENP-A(A80A81) (where the Arg 80 and Gly 81 residues were replaced by Ala 80 and Ala 81), or CENP-A(A82A83) (where the Val 82 and Asp 83 residues were replaced by Ala 82 and Ala 83), tagged with GFP. The cells were fixed with 4% paraformaldehyde 1–3 days after transfection, permeabilized, and stained with guinea pig anti-CENP-C[40] and donkey Cy5-conjugated anti-guinea pig Ig (Jackson ImmunoResearch). DNA was counterstained with 12.5 ng ml^{-1} DAPI. The fluorescence images were collected using an inverted microscope (Ti-E; Nikon) with a ×100 PlanApo VC numerical aperture (NA) = 1.4 oil-immersion objective lens, or a ×40 PlanApo NA = 0.95 dry lens, equipped with an EM-CCD camera (iXon+; Andor). The numbers of transfected cells exhibiting the GFP- or RFP-tagged protein, or both, at the centromeres were counted, and the average percentages from three independent transfections were plotted with the standard deviations.

31. Dyer, P. N. *et al.* Reconstitution of nucleosome core particles from recombinant histones and DNA. *Methods Enzymol.* **375,** 23–44 (2003).
32. Otwinowski, Z. & Minor, W. Processing of X-ray diffraction data collected in oscillation mode. *Methods Enzymol.* **276,** 307–326 (1997).
33. Collaborative Computational Project, Number 4. The *CCP*4 suite: programs for protein crystallography. *Acta Crystallogr. D* **50,** 760–763 (1994).
34. Vagin, A. & Teplyakov, A. *MOLREP*: an automated program for molecular replacement. *J. Appl. Cryst.* **30,** 1022–1025 (1997).
35. Brünger, A. T. *et al. Crystallography & NMR system*: A new software suite for macromolecular structure determination. *Acta Crystallogr. D* **54,** 905–921 (1998).
36. Emsley, P., Lohkamp, B., Scott, W. G. & Cowtan, K. Features and development of *Coot*. *Acta Crystallogr. D* **66,** 486–501 (2010).
37. Fujisawa, T. *et al.* Small-angle X-ray scattering station at the SPring-8 RIKEN beamline. *J. Appl. Cryst.* **33,** 797–800 (2000).
38. Svergun, D. I. Determination of the regularization parameter in indirect-transform methods using perceptual criteria. *J. Appl. Cryst.* **25,** 495–503 (1992).
39. Glatter, O. & Kratky, O. *Small-angle X-ray Scattering* (Academic Press, 1982).
40. Ando, S. *et al.* CENP-A, -B, and -C chromatin complex that contains the I-type α-satellite array constitutes the prekinetochore in HeLa cells. *Mol. Cell. Biol.* **22,** 2229–2241 (2002).

©2011 Macmillan Publishers Limited. All rights reserved

Supplemental Material can be found at:
http://www.jbc.org/content/suppl/2011/03/09/M110.177576.DC1.html

THE JOURNAL OF BIOLOGICAL CHEMISTRY VOL. 286, NO. 18, pp. 15678–15687, May 6, 2011
© 2011 by The American Society for Biochemistry and Molecular Biology, Inc. Printed in the U.S.A.

Oxygen Binding and Redox Properties of the Heme in Soluble Guanylate Cyclase

IMPLICATIONS FOR THE MECHANISM OF LIGAND DISCRIMINATION[*S]

Received for publication, August 20, 2010, and in revised form, January 26, 2011 Published, JBC Papers in Press, March 8, 2011, DOI 10.1074/jbc.M110.177576

Ryu Makino[‡1], Sam-yon Park[§], Eiji Obayashi[§], Tetsutaro Iizuka[¶], Hiroshi Hori[‖], and Yoshitugu Shiro[¶]

From the [‡]Department of Life Science, College of Science, Rikkyo University, Nishi-ikebukuro 3-34-1, Toshima-ku, Tokyo 171-8501, Japan, the [§]Protein Design Laboratory, Yokohama City University, 1-7-29 Suehiro, Tsurumi, Yokohama 230-0045, Japan, [¶]RIKEN Harima Institute/Spring 8, 1-1-1 Kouto, Mikazuki-cho, Sayo-gun, Hyogo 679-5148, Japan, and the [‖]Center for Quantum Science and Technology under Extreme Conditions, Osaka University, Toyonaka, Osaka 560-8531, Japan

Soluble guanylate cyclase is an NO-sensing hemoprotein that serves as a NO receptor in NO-mediated signaling pathways. It has been believed that this enzyme displays no measurable affinity for O_2, thereby enabling the selective NO sensing in aerobic environments. Despite the physiological significance, the reactivity of the enzyme-heme for O_2 has not been examined in detail. In this paper we demonstrated that the high spin heme of the ferrous enzyme converted to a low spin oxyheme (Fe^{2+}-O_2) when frozen at 77 K in the presence of O_2. The ligation of O_2 was confirmed by EPR analyses using cobalt-substituted enzyme. The oxy form was produced also under solution conditions at −7 °C, with the extremely low affinity for O_2. The low O_2 affinity was not caused by a distal steric protein effect and by rupture of the Fe^{2+}-proximal His bond as revealed by extended x-ray absorption fine structure. The midpoint potential of the enzyme-heme was +187 mV, which is the most positive among high spin protoheme-hemoproteins. This observation implies that the electron density of the ferrous heme iron is relatively low by comparison to those of other hemoproteins, presumably due to the weak Fe^{2+}-proximal His bond. Based on our results, we propose that the weak Fe^{2+}-proximal His bond is a key determinant for the low O_2 affinity of the heme moiety of soluble guanylate cyclase.

Soluble guanylate cyclase (sGC)[2] is a well characterized NO receptor involved in cell-cell signal transduction pathways associated with neuronal communication and vasodilation (1–7). Mammalian sGC is a heterodimeric ($\alpha\beta$) hemoprotein (8–10) in which the β subunit binds a stoichiometric amount of heme via a weak bond between the heme iron and His-104 (11–14). The binding of NO to the ferrous heme cleaves the weak Fe^{2+}-proximal His bond, and the resultant NO complex with 5-coordinate NO heme markedly stimulates the enzymic production of cGMP (9, 14–17). The enzyme-heme also binds carbon monoxide (CO) with moderate stimulation of enzyme activity. It has been thought that the ferrous enzyme-heme in sGC does not exhibit a measurable affinity for O_2 despite having a vacant axial position on the heme (9). This is in contrast to other hemoproteins with a Fe^{2+}-proximal His linkage, including globins and heme-containing oxygenases. The lack of affinity for O_2 allows sGC to function as a selective NO-sensor even in the presence of high concentrations of O_2 and prevents oxidation of ferrous heme by O_2.

We have examined the reaction of the enzyme-heme in sGC with external ligands using a rapid scan-stopped flow method as well as EPR, resonance Raman, and an infrared spectroscopy and established the following. (i) A 5-coordinate NO complex is produced via 6-coordinate NO complex in the reaction with NO (14). (ii) The ferric heme of sGC combines N_3^- to form a unique 5-coordinate high spin complex with a high cyclase activity (14). (iii) YC-1(3-(5′-hydroxymethyl-3′-furyl)-1-benzylindazole), an allosteric activator, induces the coordination changes in the CO complex from 6-coordinate CO heme to a 5-coordinate CO heme (17). Most of these anomalous heme coordination structures are specific to soluble guanylate cyclase among hemoproteins and seem to be associated with the weak Fe^{2+}-proximal His bond.

X-ray Structural analyses of the H-NOX (heme-NO/oxygen binding) or SONO (sensor of nitric oxide) domain, which share considerable sequence homology with the sGC heme domain, have been carried out to identify possible key determinants for modulating the O_2 binding ability of sGC (18, 19). H-NOX/SONO have a proximal His residue that is probably involved in the signaling pathway for O_2 and/or NO. Spectroscopic characterization revealed that the H-NOX/SONO heme sensor domain from *Thermoanaerobacter tengcongensis*, an obligate anaerobe, produced a 6-coordinate NO heme and a stable oxyheme (Fe^{2+}-O_2), reminiscent of globins (19, 20). By contrast, the H-NOX/SONO protein from *Clostridium botulinum* resembles mammalian and insect sGCs (21) and forms a stable 5-coordinate NO heme but not a stable oxy heme (18). The crystal structure of the oxy form of *T. tengcongensis* H-NOX revealed that a Tyr residue on the distal side of the heme was

* This work was supported by Frontier Project "Life Adaptation Strategies to Environmental Changes" of Rikkyo University and grants-in-aid from the Ministry of Culture, Education, Sports, Science, and Technology of Japan (to R. M.).

[S] The on-line version of this article (available at http://www.jbc.org) contains supplemental Figs. 1–3.

[1] To whom correspondence should be addressed: Dept. of Life Science, and Frontier Project "Life Adaptation Strategies to Environmental Changes," College of Science, Rikkyo (St. Paul's) University, Nishi-ikebukuro 3-34-1, Toshima-ku, Tokyo 171-8501, Japan. Fax: 81-3-3985-2386; E-mail: rmakino@rikkyo.ne.jp.

[2] The abbreviations used are: sGC, soluble guanylate cyclase; K_d, dissociation constant; k_{on}, association rate constant; k_{off}, dissociation rate constant; EXAFS, extended x-ray absorption fine structure; DMF, dimethylformamide; TEA, triethanolamine.

Downloaded from www.jbc.org at TSUKUBA DAIGAKU, on May 18, 2012

involved in hydrogen bond formation with the bound O_2 molecule (19). However, H-NOX proteins from facultative aerobes as well as typical NO-regulated sGCs from mammalian sources possess an Ile residue at the position corresponding to the distal Tyr (19). Replacement of the Tyr residue with Ile markedly reduced the O_2 affinity of the heme-domain of the *T. tengcongensis* protein, thereby substantiating the crucial role of the distal Tyr in the discrimination of O_2 binding in the H-NOX proteins (20).

Mammalian sGC contains Ile-145 at the position homologous to the distal Tyr. Boon *et al.* (20) converted the Ile-145 of sGC β-subunit homodimer to Tyr and found that the mutant homodimer produced a stable oxy form, although the affinity for O_2 was extremely low. Hence, it was hypothesized that the absence of a hydrogen-bonding residue in the distal heme pocket is essential for O_2 exclusion by sGC. Martin *et al.* (22) have tested the hypothesis by employing a complete human sGC heterodimer. However, substitution of Ile-145 with Tyr in the β-subunit did not facilitate the binding of O_2 to the enzyme. This unexpected finding may be due to the inappropriate orientation of the Tyr phenolic OH group relative to the ligand. Indeed, a recent publication revealed that an additional mutation, I149E, in the distal pocket enabled the enzyme-heme to react with O_2 (23). The I149E mutation probably induces a repositioning of the phenolic OH group of the introduced Tyr toward the bound O_2, facilitating the formation of a hydrogen bond. Although the above mutational study demonstrates that a hydrogen bond in the distal pocket is one of the main factors responsible for the stabilization of bound O_2, the oxy form of the mutant enzyme was still unstable and only detected as a transient species. This finding implies that an additional factor(s) might be involved in the mechanism to control the reactivity of the heme for O_2. Despite the important implication, detailed experiments to examine the reaction of sGC with O_2 have not been reported. In the present paper we describe the detection and characterization of the oxy form of sGC.

When ferrous sGC was frozen at 77 K, we found that the enzyme-heme converted to a new species with an optical spectrum similar to that of oxyhemoglobin. The new species was also produced under fluid conditions at −7 °C, but the amount was remarkably small, suggesting an extremely low O_2 affinity of the ferrous heme. This species was assigned to be an oxy form by the spectral similarity with oxymyoglobin, by the inhibitory action of isocyanide for the new species formation, and by EPR characterization of the corresponding form of the Co^{2+}-porphyrin-substituted enzyme. EXAFS analyses revealed that upon binding O_2, the ferrous iron in the out-of-plane position moved toward the heme plane without rupture of the Fe^{2+}-proximal His bond. These results indicate that the oxy form is in a 6-coordinate state and that the low affinity for O_2 is not caused by cleavage of the Fe^{2+}-proximal His bond. Electrochemical analyses revealed that the enzyme-heme had the most positive midpoint potential (+187 mV) among high spin protoheme-containing hemoproteins. This result strongly suggests that the electron density on the ferrous heme in sGC is significantly lowered relative to the ferrous heme of other hemoproteins. The decrease in the electron density, which may be due to the weak Fe^{2+}-proximal His bond, weakens the Fe^{2+}-O_2 bond strength as a result of diminished electron donation from iron to O_2. Our results suggest the weak Fe^{2+}-proximal His bond is a critical factor that could account for the lower O_2 affinity of sGC. By contrast, the distal protein effect, comprising steric hindrance in the distal heme pocket, had no significant impact on the ligand binding of sGC.

EXPERIMENTAL PROCEDURES

Enzyme Purification—Fresh bovine lung (5 kg) was minced and homogenized using a Waring blender in 15-liters of 50 mM potassium phosphate buffer, pH 7.4, containing a mixture of protease inhibitors (1 mM phenylmethylsulfonyl fluoride, 1 mM benzamidine, and 1 mM EDTA) and 55 mM β-mercaptoethanol (14, 17, 24). Protease inhibitors and β-mercaptoethanol were included in all the buffers throughout the purification unless stated otherwise. The successive purification steps of the enzyme were the same as those described earlier (24). The purified enzyme preparations were stored in liquid nitrogen until use.

Spectral Measurements—The formation of the oxy form was examined under the solution conditions at 3 and −7 °C. The experiments at subzero temperature were carried out in 40 mM TEA buffer, pH 7.5, containing 10% (v/v) ethylene glycol as antifreeze. The temperature of the cuvette holder was maintained at −7 °C or 3 °C by thermomodule elements. The fully reduced sGC was added to the anaerobic buffer solution in a septum-sealed anaerobic cuvette that was kept in an anaerobic state by flushing with N_2 gas. The optical absorption spectra under the conditions were recorded on a PerkinElmer Life Sciences Lambda 18 spectrophotometer, and 5~6 scans were averaged to improve the signal to noise ratio. After the spectra of the ferrous enzyme were collected, the solution was kept in two atmospheres of O_2 gas introduced via the septum. Optical spectra were recorded (average of 5~6 scans) after carefully shaking to equilibrate with O_2.

Optical spectra at 77 K were measured on a Shimadzu MPS-2450 spectrophotometer (Shimadzu, Kyoto, Japan) equipped with a homemade low temperature attachment consisting of a liquid N_2 Dewar and twin cuvettes (light path, 1 mm) for sample and reference solutions, as reported previously (25). To obtain a well balanced spectrum at 77 K, the buffer containing 5% ethylene glycol was employed.

EPR spectra were measured on a Varian E-12 X-band EPR spectrometer (Varian, Palo Alto, CA) with a 100-kHz field modulation. The sample temperature was controlled with an Oxford ESR-900 cryostat as described previously (14, 17).

The iron K-edge EXAFS measurements were performed using synchrotron radiation at station BLC12C of Photon Factory in the National Laboratory of High Energy Physics (Tsukuba, Japan). EXAFS data were collected at 80 K as fluorescence spectra using a 13-element germanium array detector. The results presented in this paper are the average of multiple scans. Data analyses were carried out as described previously (26–28). EXAFS, which were extracted by subtracting the background absorption, was converted to electron momentum k space, where k is a photoelectron wave vector. The resultant curve was then multiplied by k^3 to equalize the oscillation amplitude in the k space. Curve fittings were performed using the non-

Downloaded from www.jbc.org at TSUKUBA DAIGAKU, on May 18, 2012

linear least squares program EXCURV92 on the raw data weighted by k^3. Other details, including refinement of the data, are described elsewhere (26–28).

Resonance Raman spectra were measured with a JASCO NR-1800 spectrophotometer equipped with a cooled charge-coupled device detector (Princeton Instruments, Trenton, NJ). The excitation wavelength was 413.1 nm from a krypton ion laser (Coherent, Innova 90). The sample was directly mounted on an aluminum sample holder and frozen with liquid N_2. The sample holder was then inserted into the cryostat (Oxford DN1704), and the temperature of the sample was kept at 85 K with a temperature controller (Oxford ITC502).

Stopped-flow Measurements—The binding of alkyl isocyanides to the ferrous sGC was followed by a DX-18MV stopped-flow apparatus (Applied Photophysics, Leatherhead, UK). The anaerobic sGC solution was mixed with an anaerobic solution containing a desired amount of *t*-butyl or isopropyl isocyanide in the stopped-flow instrument at 20 °C. The reaction was performed under pseudo-first order conditions, and the rate constants were determined by fitting to a single exponential function using built-in software. The association rate constant (k_{on}) and dissociation rate constant (k_{off}) were determined from the slope and the *y* axis intercept, respectively, in the plot of the observed rates *versus* isocyanide concentrations.

Activity Measurements—End-point assays were performed in the cooling bath maintained at −7 °C by a Eulabo F 13 temperature controller. The assay mixture contained 470 μM GTP, 7 mM $MgCl_2$, 50 mM NaCl, 10% ethylene glycol, and an appropriate amount of the enzyme solution in 150 μl of 40 mM TEA buffer. When desired, 104 μM YC-1 or 37 μM BAY41–2272 was added to the reaction mixture supplemented with 4% DMF to maintain the solubility of YC-1 or BAY41–2272. The mixtures were equilibrated in a septum-sealed anaerobic reaction vial with 2 atmospheres of O_2 or N_2. Reactions were started by the addition of 1.5 μM native or deuteroheme-substituted sGC and conducted at −7 °C for 30 min. The reaction was terminated by the addition of 5 μl of 30% acetic acid. The amount of cGMP formed was quantified by analysis on a C18 high performance liquid chromatography column equilibrated with 20 mM potassium phosphate buffer containing 10% methanol at a constant flow rate of 1 ml/min.

Oxidation-Reduction (Redox) Potential Measurements—Spectroelectrochemical apparatus originally designed by Tsujimura *et al.* (29) was modified to enable direct monitoring of the redox potential with a platinum indicator electrode. An anaerobic 1-cm path length cuvette was used with a septum-capped port for injection and a female ground glass joint at the top that fitted to a male joint of a micro combined electrode, EA 234 (Metrohm, Herisau, Switzerland). A platinum mesh electrode (52 mesh, 8 × 10 mm) and platinum wire electrode (0.6-mm diameter) were also fixed on the inside walls of the cuvette to act as working and counter electrodes, respectively, in three-electrode potentiostat system. The combined electrode comprised a platinum indicator and Ag^+/AgCl reference electrode that was connected to a pH meter, model Accumet AR15 (Fisher), to directly monitor the electrode potentials. After the buffer solution containing mediators (1.6 ml) was introduced into the spectroelectrochemical cuvette, the combined electrode was attached to the cuvette by fitting the joints, thereby making an air-tight seal. The solution was purged with purified N_2 for 10 min. Then, the concentrated protein sample was introduced into the cuvette through the rubber septum cap. The cuvette was then placed in a temperature-controlled cell holder. The solution was constantly stirred with a magnetic stirrer during data collection. The desired redox levels of the protein sample were maintained by coulometric generation of mediator-titrant that was controlled by the three-electrode potentiostat system. The potential control by the three-electrode system was achieved by using a potentiostat, model HA-151A (Hokuto Denko Co., Tokyo, Japan). Redox potentials are quoted relative to the normal hydrogen electrode. The mediators used were 33 μM $Ru(NH_3)_6Cl_3$, 33 μM *p*-benzoquinone, 10 μM toluylene blue, and 20 μM 3′-chloroindophenol. Dithiothreitol included in the stored sGC solution was removed by passing through a Superdex 200HR column (GE Healthcare) to avoid undesired redox reactions.

Reagents—GTP, *t*-butyl isocyanide, and isopropyl isocyanide were purchased from Sigma). YC-1 was purchased from ALEXIS (San Diego, CA). Other chemicals, purchased from Wako Chemicals Co. (Tokyo, Japan), were of the highest commercial grade.

RESULTS AND DISCUSSION

Detection and Characterization of the Oxy Form at Low Temperature—We observed that the yellowish-red-colored sGC preparation in the air-saturated buffer changed to brilliant red upon freezing in liquid N_2, suggesting formation of a low spin heme. We analyzed the temperature-dependent change by low temperature optical spectroscopy at 77 K. Under anaerobic conditions, in which dissolved O_2 was removed by $Na_2S_2O_4$, the enzyme exhibited a spectrum corresponding to a high spin heme with the Soret band at ~430 nm and a broad band centered at 560 nm in the visible region at 77 K (Fig. 1*a*). By contrast, the spectrum of sGC in air-saturated buffer (*i.e.* in the absence of $Na_2S_2O_4$) at 77 K displayed well resolved α and β bands at 543 and 577 nm, respectively, accompanied by blue shift of the Soret band to 421 nm (Fig. 1*b*). Such distinct O_2-dependent spectral changes were not observed at ambient temperature (298 K) where sGC exhibited a spectrum typical of ferrous high spin heme both in the presence and absence of $Na_2S_2O_4$ at 298 K (*inset* of Fig. 1). The new species did not exhibit EPR signals assignable to ferric heme iron at either 15 and 5K. These findings together indicate that the species is in a ferrous low spin state and may be assigned to an oxy form of sGC based on the spectral similarities with that of oxyhemoglobin and the absolute requirement of O_2 for its formation. Hereafter, we interpret experimental results by assuming that the ferrous heme iron in the enzyme is capable of binding O_2 like the cobalt-substituted enzyme.

Although we have no available data to argue the mechanism of the formation, it is clear that the oxy form is produced in a course of freezing. The putative oxy form exhibited a somewhat broad Soret band with an obvious shoulder at around 430 nm and with a significant red-shifted Soret peak position in comparison with the Soret peak (417 nm) of oxyhemoglobin (Fig. 1*b*). These spectral properties suggested that the formation of

Downloaded from www.jbc.org at TSUKUBA DAIGAKU, on May 18, 2012

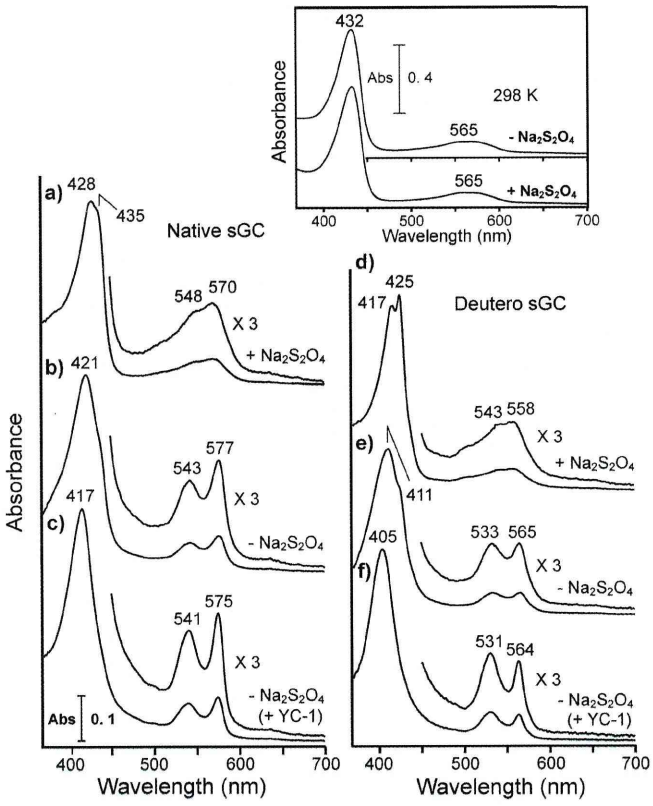

FIGURE 1. **Low temperature optical spectra of sGC.** Optical spectra of native sGC (7.1 μM) at 77 K are summarized in the *left panel*. *Trace a*, native ferrous sGC in an anaerobic buffer, in which dissolved O_2 was removed by the addition of $Na_2S_2O_4$, was frozen at 77 K, and then the spectrum was recorded. *Trace b*, shown is the spectrum of native ferrous sGC in the air-saturated buffer. *Trace c*, shown is native ferrous sGC in the air-saturated buffer containing YC-1 (104 μM). Spectra of deuteroheme-substituted enzyme at 77 K are shown in the *right panel*. *Trace d*, shown is deuteroheme-substituted sGC in the anaerobic buffer with $Na_2S_2O_4$. *Trace e*, shown is deuteroheme-substituted sGC in the air-saturated buffer. *Trace d*, shown is deuteroheme-substituted sGC in the air-saturated buffer containing YC-1 (104 μM). The buffer used was 40 mM TEA, pH 7.5, containing 5% (v/v) ethylene glycol and 50 mM NaCl. In *traces c* and *f*, 4% (v/v) DMF was supplemented in the above buffer to maintain the solubility of YC-1. The addition of DMF did not changed the spectral features both in anaerobic and aerobic conditions. In the *inset*, optical spectra of native sGC at 298 K in the presence and absence of $Na_2S_2O_4$ are shown.

the oxy form was incomplete because of the low affinity of the enzyme-heme for O_2. Likewise, complete formation of the oxy form was not observed for deuteroheme-substituted sGC despite the large increase in O_2 affinity by heme substitution as shown for myoglobin and hemoglobin (30, 31) (Fig. 1*e*). Therefore, it is unlikely that the incomplete O_2 occupation is due to the low O_2 affinity of the enzyme-heme. The complete formation of the oxy form was achieved by the addition of YC-1, as shown by a blue shift of the Soret band and intensified α and β bands (Fig. 1, *c* and *f*). These findings seem to indicate that YC-1 converts the O_2-insensitive conformation to an O_2 binding conformation.

We attempted to detect O_2 ligation at the axial position of the heme by resonance Raman spectroscopy at 80 K. Oxyhemoglobin used as control exhibited a ν_4 Raman band at 1380 cm^{-1} and a ν_3 band at 1511 cm^{-1} characteristic of 6-coordinate low spin oxy heme (data not shown). Unlike hemoglobin, sGC frozen at 80K in the air-saturated buffer exhibited only 5-coordinate high spin bands at 1358 and 1476 cm^{-1} without showing any 6-coordinate low spin Raman bands either in the presence and absence of YC-1 (data not shown). We interpreted these spectral characteristics to be caused by conversion of the 6-coordinate oxy heme to 5-coordinate heme as a result of photodissociation of the bound O_2. Thus, it was not possible to identify O_2 ligation by resonance Raman spectroscopy. Next, we tried to detect ligation of O_2 at the metal center using Co^{2+}-protoporphyrin-substituted enzyme.

We have reported that the Co^{2+}-protoporphyrin-substituted sGC has a weak Co^{2+}-His bond and produces 5-coordinate NO complex like the native sGC (14). The present experiments further established that the metal substitution has no effect on the structure as well as catalytic properties of the enzyme, because there are no significant differences in the catalytic and the nucleotide binding properties and in the subunit structure and protein surface charges between the native and the Co-substituted enzymes (supplemental Figs. 1 and 2).

The optical spectrum of Co^{2+}-proto sGC measured at 77 K in the presence of $Na_2S_2O_4$ showed a Soret band at 403 nm and 524- and 557-nm bands in the visible region (Fig. 2*A*). When frozen in the air-saturated buffer, the 557-nm band of Co^{2+}-protoporphyrin sGC was significantly decreased in intensity with an appearance of a new band at 574-nm and a significant red shift of the Soret band (Fig. 2*B*). The addition of YC-1 augmented the O_2-dependent spectral change (Fig. 2*C*). In the O_2-saturated buffer supplemented with YC-1, the spectrum converted to that of a single species with 420, 542, and 574 bands (Fig. 2*D*). These spectral features essentially agree with those of oxy Co-proto myoglobin (32). The species showed a free radical type EPR signal with hyperfine structure at $g_1 \sim 2.08$, which results from a coupling of unpaired electron to the Co nucleus (inset of Fig. 2). This is conclusive evidence for the formation of the oxy form (Co^{3+}-O_2^-) of cobalt-porphyrin (33, 34). Co^{2+}-mesoporphyrin sGC also exhibited similar O_2-dependent spectral changes (supplemental Fig. 3).

The coordination structures of the enzyme-heme in the unliganded, O_2-bound, and CO-bound states were examined by the iron K-edge EXAFS. The k^3-weighted EXAFS and the corresponding Fourier transforms are summarized in Fig. 3. To fit the experimental data, His, His and O_2, and His and CO were employed as the axial ligands for the ferrous, the O_2-bound, and the CO-bound hemes, respectively. The atomic coordination of corresponding myoglobin derivatives were employed as a starting model of the curve fitting. The structural parameters that satisfy the raw data by these approaches are summarized in Table 1. EXAFS of the unliganded ferrous sGC, obtained in the presence of $Na_2S_2O_4$ (spectrum A in the *left panel* Fig. 3), was similar to that of deoxymyoglobin (28, 35). The iron in the unliganded ferrous sGC was displaced relative to the heme plane (Fe^{2+}-Ct, distance between Fe^{2+} and porphyrin plane center) by 0.56 Å, like deoxymyoglobin (Table 1). The displacement is characteristic of high spin heme, because the high spin heme iron cannot be forced into the porphyrin plane due to the large covalent radius of high spin iron.

It is generally accepted that the Fe^{2+}-His bond strength of sGC is weaker than that of myoglobin due to strain at the heme center (13, 14, 17, 36). Although the difference in the Fe^{2+}-His

Downloaded from www.jbc.org at TSUKUBA DAIGAKU, on May 18, 2012

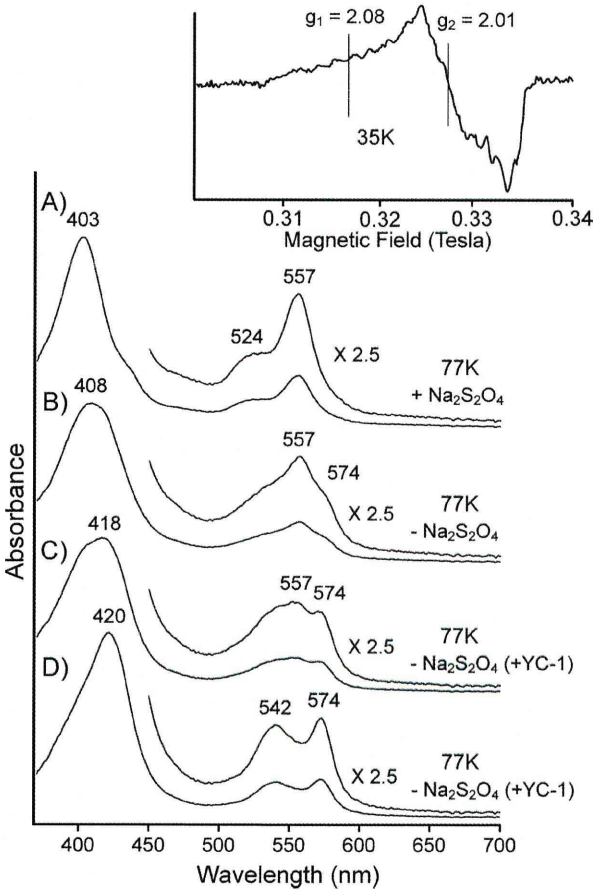

FIGURE 2. **Low temperature optical spectra of cobalt protoporphyrin-substituted sGC.** *Trace A*, Co^{2+}-protoporphyrin-substituted sGC in the anaerobic buffer in which dissolved O_2 was removed by $Na_2S_2O_4$ was frozen at 77 K, and then the spectrum was taken. *Trace B*, the spectrum of Co^{2+}-protoporphyrin-substituted sGC in the air-saturated buffer is shown. *Trace C*, the spectrum of Co^{2+}-protoporphyrin sGC in the air-saturated buffer containing YC-1(104 μM) is shown. *Trace D*, the spectrum of Co^{2+}-protoporphyrin-substituted sGC in the O_2-saturated buffer containing YC-1(104 μM) is shown. The buffer used was 40 mM TEA, pH 7.5, containing 5% (v/v) ethylene glycol and 50 mM NaCl. *Inset*, X-band (9.22 GHz) EPR spectrum of Co^{2+}-protoporphyrin-substituted sGC in the O_2-saturated buffer was taken at 35 K and by 100 K Hz field modulation with 1-millitesla width.

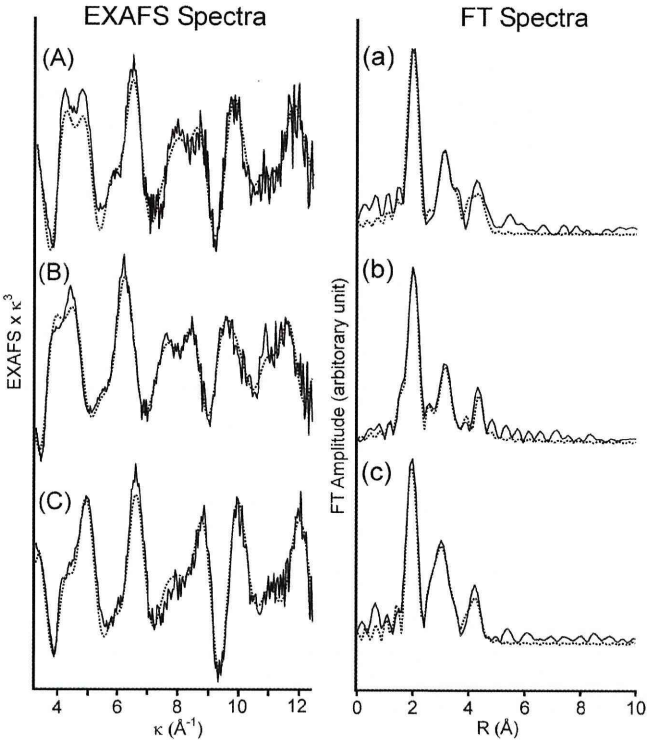

FIGURE 3. **k^3 EXAFS spectra and their Fourier transforms of sGC.** EXAFS spectra and their Fourier transforms (*FT*) were depicted in the *left* and the *right panels*, respectively. *Traces A* and *a* were in the presence of $Na_2S_2O_4$. *Traces B* and *b* were in the presence of O_2. *Traces C* and *c* were in the presence of CO. The buffer used was 40 mM TEA, pH 7.5, containing 5% (v/v) ethylene glycol and 50 mM NaCl. The enzyme concentration was 470 μM as heme. The *solid lines* indicate the observed EXAFS and Fourier transforms, and the *dashed lines* depicted simulation curves. The analyses incorporate multiple scattering from the outer shell atoms of the porphyrin ring and axial ligand molecules. Other details including refinement of data are described elsewhere (26–28).

TABLE 1

Iron-ligand distances for soluble guanylate cyclase and myoglobin in their unliganded, O_2, and CO forms estimated by EXAFS

The parameters used to simulate the K-edge EXAFS are principally the same as those by Binsted *et. al.* (26). Distances (R) and Debye-Waller terms of the ligand atom coordinating iron ($2\sigma^2$) are included in the table. The abbreviations used are: Fe^{2+}-Ct, distance of iron from the porphyrin plane center (magnitude of iron displacement); Fe^{2+}-Npyr, bond distance between iron and porphyrin nitrogen atom; Fe^{2+}-Nim, bond distance between iron and proximal His imidazole nitrogen atom; Fe^{2+}-L, bond distance between iron and sixth ligand.

	Fe^{2+}		Fe^{2+}-O_2		Fe^{2+}-CO	
Fe^{2+}-ligand site	R	$2\sigma^2$	R	$2\sigma^2$	R	$2\sigma^2$
	Å	$Å^2$	Å	$Å^2$	Å	$Å^2$
sGC						
Fe^{2+}-Ct	0.56		0.09		0.13	
Fe^{2+}-Npyr	2.09	0.004	2.09	0.002	2.05	0.003
Fe^{2+}-Nim	2.10	0.005	2.13	0.006	2.05	0.002
Fe^{2+}-L			1.89	0.004	1.85	0.004
Myoglobin						
Fe^{2+}-Ct	0.48		0.00		0.02	
Fe^{2+}-Npyr	2.05	0.004	1.99	0.002	1.99	0.004
Fe^{2+}-Nim	2.11	0.003	2.02	0.005	2.09	0.003
Fe^{2+}-L			1.85	0.004	1.81	0.003

bond strength between sGC and myoglobin was thought to be reflected in the Fe^{2+}-His bond distance, the Fe^{2+}-His bond distance observed in unliganded sGC essentially agreed with that of deoxymyoglobin (Table 1). The discrepancy may be explained by the tilting of the Fe^{2+}-imidazole nitrogen bond from the heme normal, because such a distortion also weakens the Fe^{2+}-His bond strength probably by decreasing π-bond interaction between iron $d\pi$-orbital and imidazole nitrogen $p\pi$-orbital.

EXAFS of sGC in the presence and absence of O_2 were different, indicating binding of exogenous ligand at the axial position (spectrum B in the *left panel* of Fig. 3). Placing O_2 at the 6th position of the heme using the parameters listed in Table 1, the heme iron was found to still bind the proximal His with a bond distance of 2.13 Å (Table 1). The iron displacement from the heme plane was much reduced upon placing O_2 on the heme iron (0.09 Å) (Table 1). These results showed that the proximal His moved toward the heme plane along with the movement of the heme iron to produce the 6-coordinate oxy form, and therefore, the low affinity for O_2 may be not caused by cleavage of the Fe^{2+}-His bond. In the case of the CO complex, iron displacement of the CO complex was 0.13 Å. The value was somewhat larger than that of the corresponding derivative of myoglobin

Downloaded from www.jbc.org at TSUKUBA DAIGAKU, on May 18, 2012

(Fig. 3 and Table 1), but these values fall in the range of a low spin iron.

To characterize the distal heme pocket structure, we focused on the bond distance and angle of Fe^{2+}-ligand coordination, which were obtained with multiple scattering analyses of a limited narrow *k* range EXAFS (3–13 $Å^{-1}$) (28). The geometries of sGC-ligand complexes are Fe^{2+}-O_2 bond distance = 1.89 Å and Fe^{2+}-O-O bond angle = 120° for the oxy form, and Fe^{2+}-CO bond distance = 1.85 Å and Fe^{2+}-C-O bond angle = 171 ° for the CO form. The coordination geometry for myoglobin obtained by the present curve fitting procedure was 1.85 Å (bond distance) and 104° (bond angle) for the O_2 form and 1.81 Å and 149° for the CO form. These values for myoglobin essentially agreed with those obtained by x-ray crystallographic analyses (37, 38). The present method for data analyses is useful for estimating iron-ligand geometry, although there is uncertainty in bond angle determination of ~10°, including absolute and fitting errors (28, 39). Therefore, the EXAFS studies on sGC indicate that the CO moiety of the Fe^{2+}-CO unit binds to the heme iron with a nearly linear geometry. Such geometry implies no steric protein effect on the distal side of the heme. Conversely, O_2 seems to accommodate on the distal pocket with intrinsically bent Fe^{2+}-O_2 structure.

To establish whether the ligation of O_2 affects the cyclase activity, we attempted to detect the oxy form under fluid conditions. In these experiments the formation of the oxy form was followed by the difference spectra against the spectrum in the presence of N_2. At −7 °C, the difference spectra exhibited a 410-nm peak and a 434-nm trough in the Soret region and peaks at 539 and 578 nm in the visible region (*trace a* in Fig. 4*A*). The intensity of the 410-nm peak in the difference spectrum significantly increased in the presence of YC-1 (*trace b* in Fig. 4*A*). The spectral species formed under an atmosphere of O_2 was assignable to an oxy form, because these peak and trough positions were essentially the same as those in the difference spectrum at 77 K (Fig. 4*B*). The amount of oxy form produced at −7 °C was estimated to be only 3% of total protein even in the presence of YC-1, based on the pure oxy form obtained arithmetically as described below. The formation of oxy form was temperature-dependent and significantly decreased upon raising the temperature to 3 °C (data not shown).

Deuteroheme substitution has been known to increase O_2 affinity (30, 31). As anticipated, the degree of oxy form formed at −7 °C was greater than that of the native enzyme (*trace c* in Fig. 4*A*). Nevertheless, the yield of oxy form for the deuteroheme-substituted enzyme was still only ~4%. YC-1 significantly increased the formation of the oxy form in the deuteroheme-substituted enzyme to approximately ~7% of total protein (*trace d* in Fig. 4*A*).

The effect of O_2 on cyclase activity was examined in the presence of YC-1 at −7 °C (Fig. 4*C*). The addition of NO resulted in 120-fold activation of the native enzyme, whereas the presence of O_2 did not appear to enhance the cyclase activity in the absence and presence of YC-1. Similar results were also observed for the deuteroheme-substituted enzyme, where the presence of O_2 did not enhance the cyclase activity of the substituted-enzyme in the presence of YC-1 and its derivative, BAY 41–2272 (3-(5′-hydroxymethyl-3′-furyl)-1-benzylindazole)

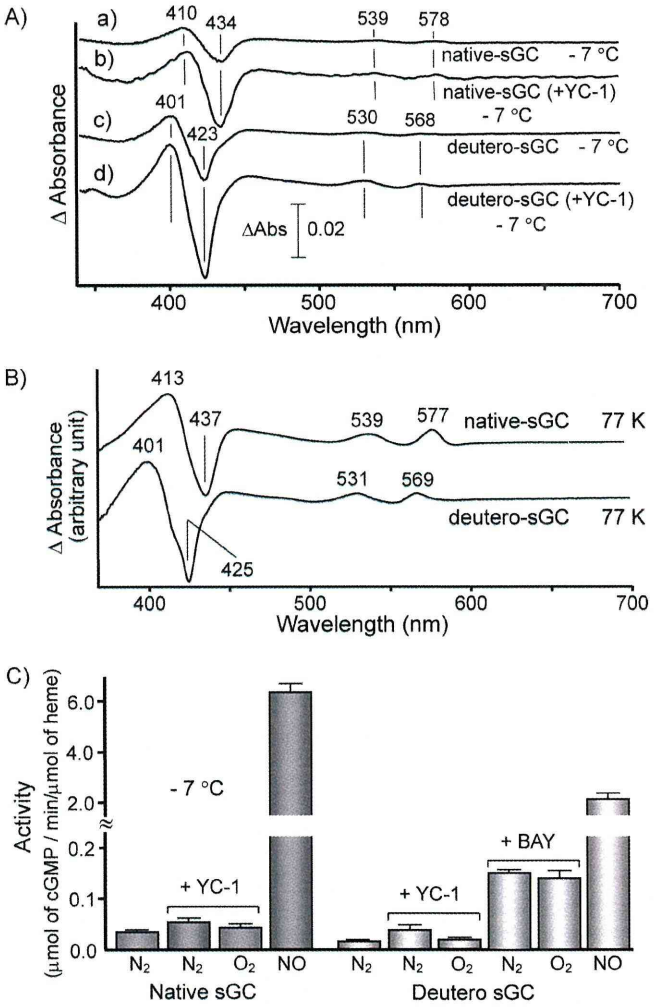

FIGURE 4. **Difference spectra of native and deuteroheme-substituted sGC between anaerobic and aerobic conditions and their cyclase activities at low temperature.** In *A*, the difference spectra between O_2 and N_2 atmosphere under fluid conditions were summarized. The enzyme samples and temperature are indicated in the figure. The enzyme concentrations were 15.1 μM in both the native and the substituted enzymes. *Traces a* and *b* were for native sGC, and *traces c* and *d* were for deuteroheme-substituted sGC. In *B*, the difference spectra between O_2 and N_2 atmosphere under frozen conditions at 77 K are illustrated. The difference spectra shown were obtained by subtracting the spectrum under N_2 atmosphere from that under O_2 atmosphere. In *C*, activities of native and deuteroheme-substituted enzymes were assayed in 40 mM TEA, pH 7.5, containing 10% ethylene glycol, 50 mM NaCl, 7 mM $MgCl_2$, and 0.47 mM GTP. When the addition of YC-1 (104 μM) or BAY 41–2272 (40 μM) was desired, 4% DMF was supplemented to the above buffer to maintain the solubility. The effect of DMF on the basal and NO-stimulated activities was negligible under the experimental conditions.

(Fig. 4*C*). In this connection it is interesting to note that the cyclase activity catalyzed by Gcy-88E from *Drosophila* was not stimulated by CO, NO, and O_2 (40). This enzyme formed stable 6-coordinate NO and O_2 complex, unlike typical sGC. These results together with the present data suggest that the ligand-dependent stimulation may be closely coupled with the Fe^{2+}-His bond strength, although the detailed mechanism remains to be elucidated.

To ask whether the exogenous heme-ligand can prevent O_2 binding to the enzyme-heme, we examined the inhibitory effect on the O_2 binding. As shown in Fig. 5*A*, the O_2-dependent spectral change in the presence of BAY 41–2272 yielded the

Downloaded from www.jbc.org at TSUKUBA DAIGAKU, on May 18, 2012

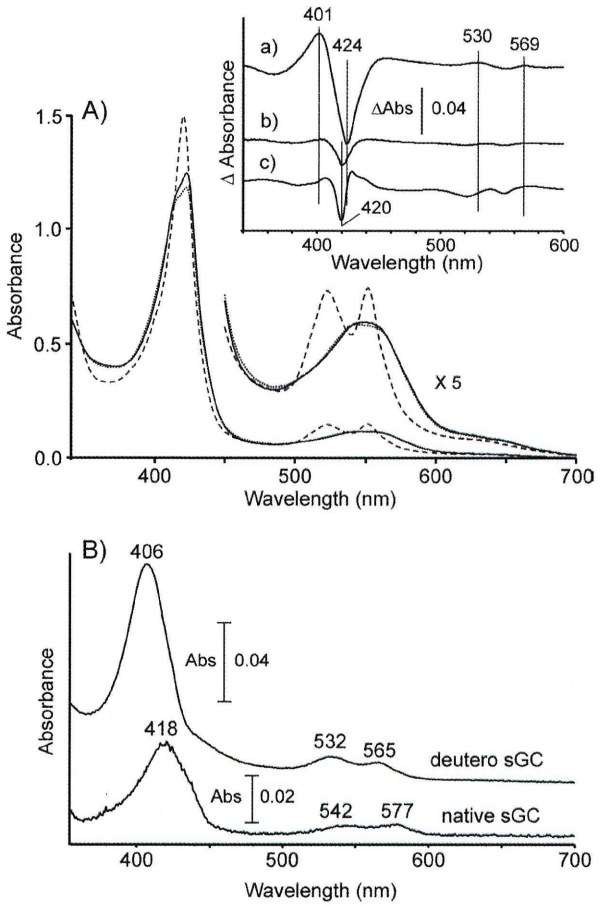

FIGURE 5. **The effect of isocyanide on the O_2 binding and the spectra of the complete oxy form.** In *A*, the optical spectra of deuteroheme-substituted sGC in the presence of BAY 41–2272 were illustrated. The spectra shown by a *solid* and a *dotted line* are the spectrum of the ferrous enzyme in the N_2-saturated and in the O_2-saturated buffer, respectively. The spectrum shown by the *broken line* was that in the presence of isopropyl isocyanide (170 μM). The buffer used was 40 mM TEA buffer, pH 7.5, containing 10% ethylene glycol, 50 mM NaCl, 4% DMF, and 37 μM BAY 41–2272. The difference spectra were summarized in the *inset*, where *trace a* is a difference spectrum by subtracting the spectrum in the N_2-saturated buffer from that in the O_2-saturated buffer, and *trace* b was obtained by subtracting the spectrum in the N_2 buffer from that in the O_2 buffer, of which buffers contained isopropyl isocyanide (170 μM). *Trace c* is the difference spectrum by subtracting the spectrum of the isopropyl isocyanide adduct from that of the ferrous enzyme, which is illustrated in the 1/10 scale. In *B*, the spectrum of the complete oxy form was arithmetically obtained by subtracting the ferrous spectrum multiplied by a factor from the spectrum in the O_2-saturated buffer. The data used for the native enzyme were the absolute spectra (in N_2 and O_2) used to generate *trace b* in Fig. 4*A* and for the deuteroheme-substituted enzyme the spectra in Fig. 5*A*. The subtractions of the ferrous enzyme multiplied by 0.97 and 0.89 could satisfactorily eliminate the residual ferrous enzyme for the native and the deuteroheme enzymes, respectively.

largest change observed so far (compare the *solid line* with the *dotted line*). In contrast, the O_2-dependent spectral change was noted to be much reduced when isopropyl isocyanide was included in the mixture (compare *trace a* with *trace b* in the *inset* of Fig. 5*A*). The difference spectrum (*trace b*) does not agree with *trace a* in the entire spectral region. Although the *trace b* displayed the trough at 420 nm similar to that of *trace c*, the bandwidth of *trace b* was much larger than that of *trace c*, suggesting the displacement of the bound isocyanide by O_2. The nearly identical result was also observed for native sGC in the reaction of the *t*-butyl isocyanide adduct with O_2 (data not shown). These spectral features agreed with the view that isocyanide competed with the same site as O_2.

The spectrum of the complete oxy form could be arithmetically obtained by subtracting the ferrous-enzyme spectrum multiplied by a factor from the spectrum in the O_2-saturated buffer. In the presence of YC-1 and BAY 41–2272, as shown in Fig. 5*A*, the subtractions of the ferrous enzyme multiplied by 0.97 and 0.89 could satisfactorily eliminate the residual ferrous enzyme for the native and the deuteroheme enzyme, respectively. The resultant arithmetic spectra (Fig. 5*B*) agree with those of the oxy form obtained at 77K (Fig. 1). On the basis of these results together with EXAFS and other optical spectral studies described in this paper, we finally conclude that the heme in sGC is capable of binding O_2.

Protein Effects on Ligand Binding—Using the systematic kinetic data, Mims *et al.* (41) assessed the protein effects on the ligand binding of myoglobin. The effects are summarized as (i) distal steric hindrance to restrict the approach of the ligand to its final position and (ii) a protein proximal effect that controls successive bond formation of the iron with ligand on the distal side. When the bond between iron and ligand (such as O_2) is generated, the distal His residue forms a hydrogen bond with the bound O_2 to stabilize the O_2 complex. These mechanisms, which were originally formulated for myoglobin, provide key clues in understanding the ligand binding of other hemoproteins.

We have assessed the distal steric protein effect by analyzing the reaction of the ferrous heme iron with alkyl isocyanides. As shown in Fig. 6*A*, careful titration with *t*-butyl isocyanide showed that the unliganded ferrous sGC converted to the isocyanide adduct through one set of isosbestic points. The binding of isopropyl isocyanide also yielded nearly identical species (data not shown). The optical spectra of these alkyl isocyanide adducts were essentially the same as those of the corresponding isocyanide adducts of myoglobin, demonstrating that the isocyanide adducts of sGC were in a six-coordinate low spin state (42). The dissociation constants (K_d) calculated were 46 and 90 μM for *t*-butyl isocyanide and isopropyl isocyanide (*inset* of Fig. 6), respectively, indicating that the affinity for *t*-butyl isocyanide is significantly higher by comparison to that for isopropyl isocyanide. In general, the affinities of isocyanide for the hemoproteins decreased with increasing size of alkyl group in the isocyanide molecule (41). In contrast, sGC exhibited a higher affinity for isocyanide with a larger alkyl group. The anomalous property has also been noted for human hemeoxygenase (43). The association rates of isocyanides with the ferrous sGC decreased with increasing size of alkyl group in the isocyanide molecule. The rates are 10-fold faster than the formation of the corresponding isocyanide adducts of myoglobin (Fig. 6*B* and Table 2) and nearly equivalent to those of leghemoglobin (44), which are the highest among the globin family. Taking into consideration these findings, we propose that there is no substantial resistance to the binding of bulky isocyanides with sGC, in contrast to myoglobin, supporting the previous result (45).

In accordance with a previous report (22), sGC binds CO with an association rate constant of $3.6 \times 10^4\ M^{-1}\ s^{-1}$, which is particularly slow among 5-coordinate high spin hemoproteins (Table 2). The most striking feature is that the association rate

Downloaded from www.jbc.org at TSUKUBA DAIGAKU, on May 18, 2012

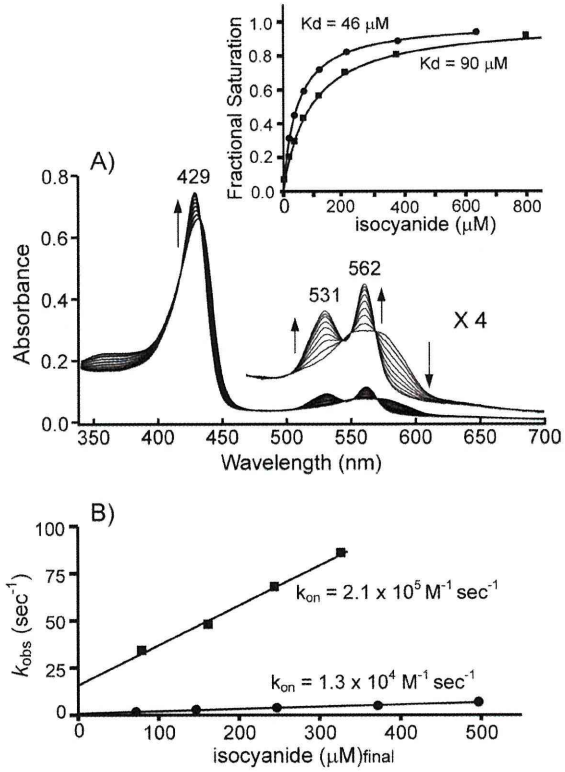

FIGURE 6. **Equilibrium binding and kinetic analyses of alkyl isocyanide binding.** *A*, shown are changes in the absorption spectra of sGC during titration with *t*-butyl isocyanide. *B*, k_{obs} values obtained from stopped-flow traces were plotted against the final concentration of isocyanide after mixing. Closed circles (●) are data from *t*-butyl isocyanide, and closed squares (■) are data from isopropyl isocyanide. In the *inset*, isocyanide binding curves are plotted as the fractional saturation *versus* the effective concentration of isocyanide. *Solid lines* depicted simulated lines obtained by nonlinear regression analyses. Equilibrium and kinetic binding experiments were done at 20 °C. Other details are described under "Experimental Procedures."

TABLE 2

Ligand binding properties of soluble guanylate cyclase, sperm whale myoglobin, and soybean leghemoglobin

	K_d	k_{on}	K_{off}	Reference
	μM	M^{-1} s^{-1}	s^{-1}	
Soluble guanylate cyclase				
CO	298[a]	3.6×10^4	10.7	This study
Isopropyl isocyanide	90 (81[a])	2.0×10^5	16.1	This study
t-Butyl isocyanide	48 (61[a])	1.3×10^4	0.80	This study
Sperm whale myoglobin				
CO	0.03[a]	5.0×10^5	0.015	41
Isopropyl isocyanide	73 (87[a])	7.5×10^3	0.65	This study
t-Butyl isocyanide	836 (803[a])	1.5×10^3	1.20	This study
Soybean leghemoglobin				
CO	0.0013[a]	1.3×10^7	0.016	44
Isopropyl isocyanide	0.0073[a]	4.1×10^5	0.0030	44
t-Butyl isocyanide	0.082[a]	2.2×10^4	0.0018	44

[a] Calculated as k_{off}/k_{on}.

for isopropyl isocyanide was approximately one order of magnitude faster than that for CO binding, irrespective of the larger size of the isocyanide by comparison to CO (Table 2). These findings strongly suggest that sGC permits easy access for small ligands, such as CO and O_2, to the coordination position. Therefore, the formation of the coordinate bond dominates the kinetics of association, accentuating the significance of the proximal protein effect.

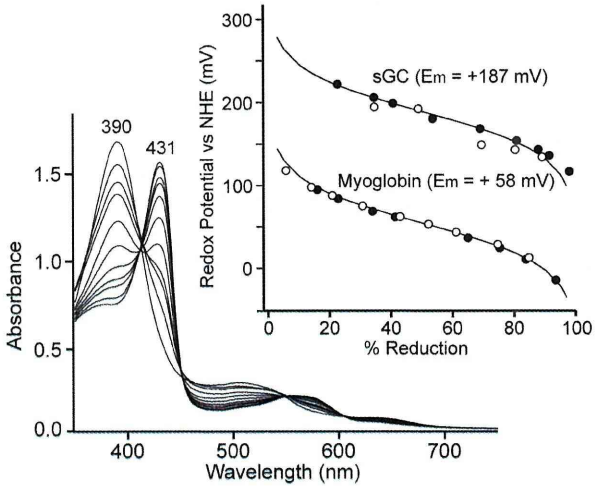

FIGURE 7. **Anaerobic redox titration of sGC.** The reaction mixture contained 15 μM of sGC or sperm whale myoglobin and a mixture of mediators in 50 mM Hepes buffer at pH 7.5 containing 50 mM KCl and 5% ethylene glycol. The final volume was 1.6 ml. The cuvette was kept under an anaerobic atmosphere of N_2, at 20 °C. The desired redox levels were maintained by coulometric generation of mediator-titrant, of which potentials were controlled by a three-electrode system as described in under "Experimental Procedures." After the reaction was achieved to redox equilibrium, spectra were recorded. Redox potentials were determined by both the reductive (○) and oxidative (●) titrations, in which the potentials were directly monitored by a combined microelectrode. In the *inset*, redox potentials were plotted against the degree of reduction. *Solid lines* denote the theoretical lines calculated according to Nernst equation with $n = 1$. Other details were described under "Experimental Procedures." Mediators used were 17 μM pyocyanine, 2 μM 2,6-dichloroindophenol, 6.6 μM toluylene blue, and 33 μM $Ru(NH_3)_6Cl_3$ for myoglobin and 33 μM *p*-benzoquinone, 33 μM $Ru(NH_3)_6Cl_3$, 10 μM toluylene blue, and 20 μM 3′-chloroindophenol for sGC. *NHE* denotes Normal Hydrogen Electrode.

Based on quantum mechanical and molecular mechanical analyses, it was proposed that the degree of electron density on the heme iron might be controlled by the protein proximal effect (46). This effect on the proximal side modulates the Fe^{2+}-ligand bond formation on the distal side. For instance, when the Fe^{2+}-proximal His bond is weakened by strain imposed on the bond, the electron density on the heme iron is reduced relative to that of the Fe^{2+}-His bond without strain. This might reduce the electron donation from the iron to ligand such as O_2, resulting in the weakening of the Fe^{2+}-O_2 bond strength (46). Thus, a weak Fe^{2+}-His bond correlates with a weak Fe^{2+}-O_2 bond and vice versa. Such a protein effect, referred to as a positive *trans* effect, accounts for the unique character of the CO and O_2 binding characteristics of the iron-porphyrin complexes (47–50). The proximal effect derived by strain on the Fe^{2+}-His bond probably affects redox potential of the heme, because the decrease in electron density at the ferrous heme makes it more difficult to remove an electron (51). For example, T-state hemoglobin with a more strained Fe^{2+}-His bond and lower O_2 affinity relative to R-state hemoglobin exhibited significantly higher midpoint potentials of the heme than R-state hemoglobin (52). The redox potential measurements of sperm whale myoglobin and sGC indicated that the electrochemical titration curves fitted to a Nernst equation with $n = 1$ in both hemoproteins (Fig. 7). The ferric-ferrous couple of myoglobin gave the midpoint potential of +58 mV, in reasonable agreement with the reported value. The midpoint potential of sGC, +187 mV, was considerably higher than that

Downloaded from www.jbc.org at TSUKUBA DAIGAKU, on May 18, 2012

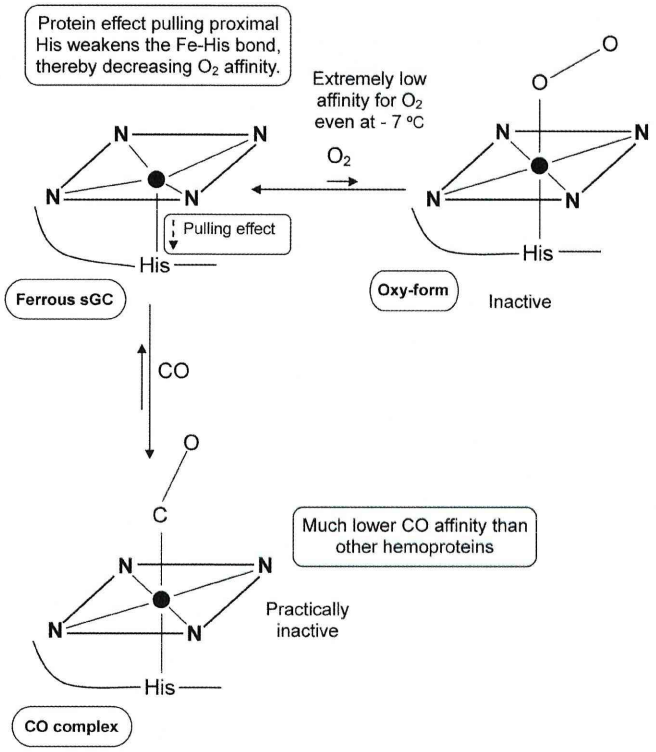

FIGURE 8. **Model proposed for bindings of the ferrous sGC with O_2 and CO.** The heme coordination structures were depicted based on EXAFS data (Table 1). *Closed circles* illustrated in the center of heme denote ferrous iron atom. The weak Fe^{2+}-His bond in the ferrous enzyme may decrease charge density on the heme iron, thereby decreasing the O_2 affinity and elevating the redox potential of the heme.

of myoglobin. It should be noted that the measured value was the most positive among high spin protoheme-containing hemoproteins, presumably because the electron density of the heme in sGC is significantly reduced by the protein proximal effect. Based on the above considerations and EXAFS data, the significance of the proximal protein effect on the ligand binding was noted as summarized in Fig. 8.

In summary, we have detected and characterized the oxy form of sGC. To assess the crucial determinant(s) for the low O_2 affinity of sGC, we have analyzed the coordination structure by EXAFS. Our results indicate that the low affinity for O_2 is not caused by cleavage of the Fe^{2+}-proximal His bond. Among protein effects to regulate the reactivity of heme, the distal steric hindrance could be excluded based on the kinetic studies. The critical factor that may contribute to the low O_2 affinity is the protein proximal effect, a regulatory effect caused by the weak Fe^{2+}-proximal His bond. Measurement of the midpoint potential of the heme also highlights the significance of the protein proximal effect in terms of the unique low O_2 affinity of sGC. Based on the findings described in this paper, we to propose that the weak Fe^{2+}-proximal His bond is a key factor in regulating the reactivity of the heme in sGC along with the hydrogen bond interaction in the distal pocket, which was identified previously by mutational analysis (20).

REFERENCES

1. Furchgott, R. F., and Zawadzki, J. V. (1980) *Nature* **288,** 373–376
2. Ignarro, L. J., and Kadowitz, P. J. (1985) *Annu. Rev. Pharmacol. Toxicol.* **25,** 171–191
3. Waldman, S. A., and Murad, F. (1987) *Pharmacol. Rev.* **39,** 163–196
4. Garthwaite, J., Charles, S. L., and Chess-Williams, R. (1988) *Nature* **336,** 385–388
5. Bredt, D. S., and Snyder, S. H. (1989) *Proc. Natl. Acad. Sci. U.S.A.* **86,** 9030–9033
6. Moncada, S., and Higgs, E. A. (1991) *Eur. J. Clin. Invest.* **21,** 361–374
7. Verma, A., Hirsch, D. J., Glatt, C. E., Ronnett, G. V., and Snyder, S. H. (1993) *Science* **259,** 381–384
8. Kamisaki, Y., Saheki, S., Nakane, M., Palmieri, J. A., Kuno, T., Chang, B. Y., Waldman, S. A., and Murad, F. (1986) *J. Biol. Chem.* **261,** 7236–7241
9. Stone, J. R., and Marletta, M. A. (1994) *Biochemistry* **33,** 5636–5640
10. Humbert, P., Niroomand, F., Fischer, G., Mayer, B., Koesling, D., Hinsch, K. D., Gausepohl, H., Frank, R., Schultz, G., and Böhme, E. (1990) *Eur. J. Biochem.* **190,** 273–278
11. Wedel, B., Humbert, P., Harteneck, C., Foerster, J., Malkewitz, J., Böhme, E., Schultz, G., and Koesling, D. (1994) *Proc. Natl. Acad. Sci. U.S.A.* **91,** 2592–2596
12. Zhao, Y., and Marletta, M. A. (1997) *Biochemistry* **36,** 15959–15964
13. Deinum, G., Stone, J. R., Babcock, G. T., and Marletta, M. A. (1996) *Biochemistry* **35,** 1540–1547
14. Makino, R., Matsuda, H., Obayashi, E., Shiro, Y., Iizuka, T., and Hori, H. (1999) *J. Biol. Chem.* **274,** 7714–7723
15. Ignarro, L. J., Wood, K. S., and Wolin, M. S. (1982) *Proc. Natl. Acad. Sci. U.S.A.* **79,** 2870–2873
16. Gerzer, R., Hofmann, F., and Schultz, G. (1981) *Eur. J. Biochem.* **116,** 479–486
17. Makino, R., Obayashi, E., Homma, N., Shiro, Y., and Hori, H. (2003) *J. Biol. Chem.* **278,** 11130–11137
18. Nioche, P., Berka, V., Vipond, J., Minton, N., Tsai, A. L., and Raman, C. S. (2004) *Science* **306,** 1550–1553
19. Pellicena, P., Karow, D. S., Boon, E. M., Marletta, M. A., and Kuriyan, J. (2004) *Proc. Natl. Acad. Sci.* **101,** 12854–12859
20. Boon, E. M., Huang, S. H., and Marletta, M. A. (2005) *Nat. Chem. Biol.* **1,** 53–59
21. Hu, X., Murata, L. B., Weichsel, A., Brailey, J. L., Roberts, S. A., Nighorn, A., and Montfort, W. R. (2008) *J. Biol. Chem.* **283,** 20968–20977
22. Martin, E., Berka, V., Bogatenkova, E., Murad, F., and Tsai, A. L. (2006) *J. Biol. Chem.* **281,** 27836–27845
23. Derbyshire, E. R., Deng, S., and Marletta, M. A. (2010) *J. Biol. Chem.* **285,** 17471–17478
24. Yazawa, S., Tsuchiya, H., Hori, H., and Makino, R. (2006) *J. Biol. Chem.* **281,** 21763–21770
25. Hagihara, B., and Iizuka, T. (1971) *J. Biochem.* **69,** 355–362
26. Binsted, N., Strange, R. W., and Hasnain, S. S. (1992) *Biochemistry* **31,** 12117–12125
27. Obayashi, E., Tsukamoto, K., Adachi, S., Takahashi, S., Nomura, M., Iizuka, T., Shoun, H., and Shiro, Y. (1997) *J. Am. Chem. Soc.* **119,** 7807–7816
28. Miyatake, H., Mukai, M., Adachi, S., Nakamura, H., Tamura, K., Iizuka, T., Shiro, Y., Strange, R. W., and Hasnain, S. S. (1999) *J. Biol. Chem.* **274,** 23176–23184
29. Tsujimura, S., Kuriyama, A., Fujieda, N., Kano, K., and Ikeda, T. (2005) *Anal. Biochem.* **337,** 325–331
30. Makino, R., and Yamazaki, I. (1974) *Arch. Biochem. Biophys.* **165,** 485–493
31. Seybert, D. W., Moffat, K., Gibson, Q. H., and Chang, C. K. (1977) *J. Biol. Chem.* **252,** 4225–4231
32. Yonetani, T., Yamamoto, H., and Woodrow, G. V., 3rd (1974) *J. Biol. Chem.* **249,** 682–690
33. Ikeda-Saito, M., Iizuka, T., Yamamoto, H., Kayne, F. J., and Yonetani, T. (1977) *J. Biol. Chem.* **252,** 4882–4887
34. Hori, H., Ikeda-Saito, M., and Yonetani, T. (1982) *J. Biol. Chem.* **257,** 3636–3642
35. Eisenberger, P., Shulman, R. G., Kincaid, B. M., Brown, G. S., and Ogawa, S. (1978) *Nature* **274,** 30–34
36. Stone, J. R., Sands, R. H., Dunham, W. R., and Marletta, M. A. (1995) *Biochem. Biophys. Res. Commun.* **207,** 572–577
37. Li, T., Quillin, M. L., Phillips, G. N., Jr., and Olson, J. S. (1994) *Biochemistry*

Downloaded from www.jbc.org at TSUKUBA DAIGAKU, on May 18, 2012

33, 1433–1446
38. Yang, F., and Phillips, G. N., Jr. (1996) *J. Mol. Biol.* **256,** 762–774
39. Rich, A. M., Armstrong, R. S., Ellis, P. L., and Lay, P. A. (1998) *J. Am. Chem. Soc.* **120,** 10827–10836
40. Huang, S. H., Rio, D. C., and Marletta, M. A. (2007) *Biochemistry* **46,** 15115–15122
41. Mims, M. P., Porras, A. G., Olson, J. S., Noble, R. W., and Peterson, J. A. (1983) *J. Biol. Chem.* **258,** 14219–14232
42. Derbyshire, E. R., and Marletta, M. A. (2007) *J. Biol. Chem.* **282,** 35741–35748
43. Evans, J. P., Kandel, S., and Ortiz de Montellano, P. R. (2009) *Biochemistry* **48,** 8920–8928
44. Stetzkowski, F., Cassoly, R., and Banerjee, R. (1979) *J. Biol. Chem.* **254,** 11351–11356
45. Derbyshire, E. R., Tran, R., Mathies, R. A., and Marletta, M. A. (2005) *Biochemistry* **44,** 16257–16265
46. Marti, M. A., Crespo, A., Capece, L., Boechi, L., Bikiel, D. E., Scherlis, D. A., and Estrin, D. A. (2006) *J. Inorg. Biochem.* **100,** 761–770
47. Collman, J. P., Brauman, J. I., Iverson, B. L., Seeler, J. L., Morris, R. M., and Gibson, Q. M. (1983) *J. Am. Chem. Soc.* **105,** 3052–3064
48. Oberting, W. A., Kean, R. T., Wever, R., and Babcock, G. T. (1990) *Inorg. Chem.* **29,** 2633–2645
49. Traylor, T. G., Duprat, A. F., and Sharma, V. S. (1993) *J. Am. Chem. Soc.* **115,** 810–811
50. Gullotti, M., Santagostini, L., Monzani, E., and Casella, L. (2007) *Inorg. Chem.* **46,** 8971–8975
51. Falk, J. E. (1964) *Porphyrins and Metalloporphyrins,* pp. 67–71, Elsevier Publishing Co., Amsterdam
52. Faulkner, K. M., Bonaventura, C., and Crumbliss, A. L. (1995) *J. Biol. Chem.* **270,** 13604–13612

Downloaded from www.jbc.org at TSUKUBA DAIGAKU, on May 18, 2012

ARTICLE
Journal of Cellular Biochemistry 113:808–814 (2012)

Journal of Cellular Biochemistry

Identification and Functional Analysis of Zranb2 as a Novel Smad-Binding Protein That Suppresses BMP Signaling

Satoshi Ohte,[1] Shoichiro Kokabu,[1] Shun-ichiro Iemura,[2] Hiroki Sasanuma,[1] Katsumi Yoneyama,[1] Masashi Shin,[1] Seiya Suzuki,[1] Toru Fukuda,[1] Yukio Nakamura,[3] Eijiro Jimi,[4] Toru Natsume,[2] and Takenobu Katagiri[1*]

[1] *Division of Pathophysiology, Research Center for Genomic Medicine, Saitama Medical University, 1397-1 Yamane, Hidaka-shi, Saitama, 350-1241, Japan*

[2] *Biological Systems Control Team, Biomedicinal Information Research Center, National Institute of Advanced Industrial Science and Technology, 2-42 Aomi, Koto-ku, Tokyo, 135-0064, Japan*

[3] *Showa Inan General Hospital, 3230 Akaho, Komagane-shi, Nagano, 399-4117, Japan*

[4] *Department of Biosciences, Kyushu Dental College, Kitakyushu-shi, Fukuoka, 803-8580, Japan*

ABSTRACT

Smads 1/5/8 transduce the major intracellular signaling of bone morphogenetic proteins (BMPs). In the present study, we analyzed Smad1-binding proteins in HEK293T cells using a proteomic technique and identified the protein, zinc-finger, RAN-binding domain-containing protein 2 (ZRANB2). Zranb2 interacted strongly with Smad1, Smad5, and Smad8 and weakly with Smad4. The overexpression of Zranb2 inhibited BMP activities in C2C12 myoblasts *in vitro*, and the injection of Zranb2 mRNA into zebrafish embryos induced weak dorsalization. Deletion analyses of Zranb2 indicated that the serine/arginine-rich (SR) domain and the glutamine-rich domain were required for the inhibition of BMP activity and the interaction with Smad1, respectively. Zranb2 was found to be localized in the nucleus; however, the SR domain-deleted mutant localized to the cytoplasm. The knockdown of endogenous Zranb2 in C2C12 cells enhanced BMP activity. Zranb2 suppressed Smad transcriptional activity without affecting Smad phosphorylation, nuclear localization, or DNA binding. Taken together, these findings suggested that Zranb2 is a novel BMP suppressor that forms a complex with Smads in the nucleus. J. Cell. Biochem. 113: 808–814, 2012. © 2011 Wiley Periodicals, Inc.

KEY WORDS: BMP; SMAD; ZRANB2; PROTEIN INTERACTION; SIGNAL TRANSDUCTION

Bone morphogenetic proteins (BMPs) are multifunctional growth factors that are members of the transforming growth factor-β family. BMPs exhibit a unique activity in bone matrix that is characterized by ectopic bone formation in muscle tissues *in vivo* [Urist, 1965]. BMPs inhibit the myogenic differentiation of myoblasts and cause an osteogenic differentiation into osteoblastic lineage cells *in vitro* [Katagiri et al., 1994]. BMPs physiologically regulate bone formation and the development and regeneration of various tissues in vertebrates and lower animals [Katagiri et al., 2008]. In zebrafish and Xenopus embryos, BMP signaling plays an important role in the determination of a dorsal–ventral axis during development [Suzuki et al., 1994; Nakamura et al., 2007].

BMP signaling is transduced using two different transmembrane serine/threonine kinase receptors, which are termed type I and type II receptors [Miyazono et al., 2005; Wan and Cao, 2005]. The BMP-bound type II receptor phosphorylates the type I receptor. The activated BMP type I receptor kinase subsequently phosphorylates a serine–valine–serine (SVS) motif at the C-termini of Smad1, Smad5, and Smad8, which are the BMP receptor-regulated Smads (R-Smads) [Katagiri, 2010]. The phosphorylated R-Smads form heteromeric complexes with Smad4, which is a common Smad (Co-Smad), and translocate into the nucleus to regulate the transcription of direct target genes, such as *Id1* [Katagiri et al., 2002]. A GC-rich element in the 5′ enhancer region of the *Id1* gene has been identified as the BMP-responsive element (BRE), which is recognized by a complex of BMP-regulated Smads and Smad4 in response to activation of the BMP type I receptor. The overexpression of a constitutively active Smad1, in which the SVS motif has been substituted with a DVD

Grant sponsor: Ministry of Health, Labour and Welfare of Japan; Grant number: H23-nanchi-ippan-032; Grant sponsor: Ministry of Education, Culture, Sports, Science, and Technology of Japan; Grant numbers: 21390423, 23659732, 21890243, S0801004; Grant sponsor: Takeda Science Foundation; Grant number: 2009-Katagiri.

*Correspondence to: Takenobu Katagiri, Division of Pathophysiology, Research Center for Genomic Medicine, Saitama Medical University, 1397-1 Yamane, Hidaka-shi, Saitama, 350-1241, Japan. E-mail: katagiri@saitama-med.ac.jp

Received 8 September 2011; Accepted 6 October 2011 • DOI 10.1002/jcb.23408 • © 2011 Wiley Periodicals, Inc.
Published online 20 October 2011 in Wiley Online Library (wileyonlinelibrary.com).

sequence, activates the expression of the *Id1* reporter gene and the osteoblastic differentiation of myoblasts in the absence of BMPs [Nojima et al., 2010]. Moreover, a chemical inhibitor of BMP type I receptor-mediated R-Smad phosphorylation suppressed BMP receptor-mediated osteoblastic differentiation and heterotopic bone formation [Yu et al., 2008a, b]. These findings suggest that Smads play a critical role in BMP activities both *in vitro* and *in vivo*.

The activity of Smad proteins is regulated via interactions with various factors, including modifying enzymes, co-activators, and co-repressors [Miyazono et al., 2006]. The Smads are degraded by binding to the ubiquitin–proteasome system *via* interactions with E3 ubiquitin ligases, such as Smad ubiquitin regulatory factors 1 and 2 (Smurf1 and Smurf2) [Zhu et al., 1999]. In addition, two distinct phosphatases, small C-terminal domain phosphatases (SCPs) and protein phosphatase magnesium-dependent 1A (PPM1A), have been identified as enzymes that stimulate the dephosphorylation of Smads [Knockaert et al., 2006; Lin et al., 2006]. In the nucleus, Smads interact with various transcriptional co-activators, including p300, CBP, and PCAF [Feng et al., 1998; Itoh et al., 2000], and co-repressors, including Ski, SnoN, and YY1 [Akiyoshi et al., 1999; Wu et al., 2002; Kurisaki et al., 2003]. Thus, the identification and characterization of novel Smad-binding proteins are important to understand the mechanisms of the Smad signaling pathway. In the present study, we report the identification and characterization of a protein, zinc-finger, RAN-binding domain containing protein 2 (Zranb2), as a factor that binds BMP-regulated R-Smads. Zranb2, also known as Zis and Znf265, was identified previously in renal juxtaglomerular cells [Karginova et al., 1997]. Zranb2 contains two RanBP2-type zinc-finger domains, a glutamic acid-rich (Glu) region and a C-terminal Ser/Arg-rich (SR) domain [Mangs and Morris, 2008]. Zranb2 is involved in the alternative splicing of RNA through the zinc-finger domains in a reconstituted assay *in vitro* [Adams et al., 2001]. The current study is the first report to demonstrate that Zranb2 acts as a BMP inhibitor by suppressing Smad transcriptional activity without affecting Smad phosphorylation or DNA-binding capacity.

RESULTS

ZRANB2 INTERACTS WITH BMP-REGULATED SMADS

To identify novel proteins that regulate BMP signaling *via* the Smads, we analyzed Smad1-binding proteins using a proteomic technique. FLAG-Smad1 was overexpressed in HEK293T cells, and the Smad1-binding proteins were enriched from whole-cell extracts using immunoprecipitation with an anti-FLAG antibody. ZRANB2 was identified as a Smad1-binding protein (Fig. 1A). Myc-tagged Zranb2 interacted with FLAG-Smad1 and weakly interacted with FLAG-Smad4 in HEK293T cells (Fig. 1B), and this binding capacity of Zranb2 to Smad1 was not affected by BMP-4 stimulation (Fig. 1C). In addition, Zranb2 interacted with two other BMP-regulated R-Smads, Smad5 and Smad8 (Fig. 1D).

ZRANB2 INHIBITS BMP ACTIVITIES VIA SMADS

We examined the effect of Zranb2 on BMP activities in C2C12 myoblasts, a well-characterized model system for studying the biological activity of BMPs [Katagiri et al., 1994]. The ALP activity

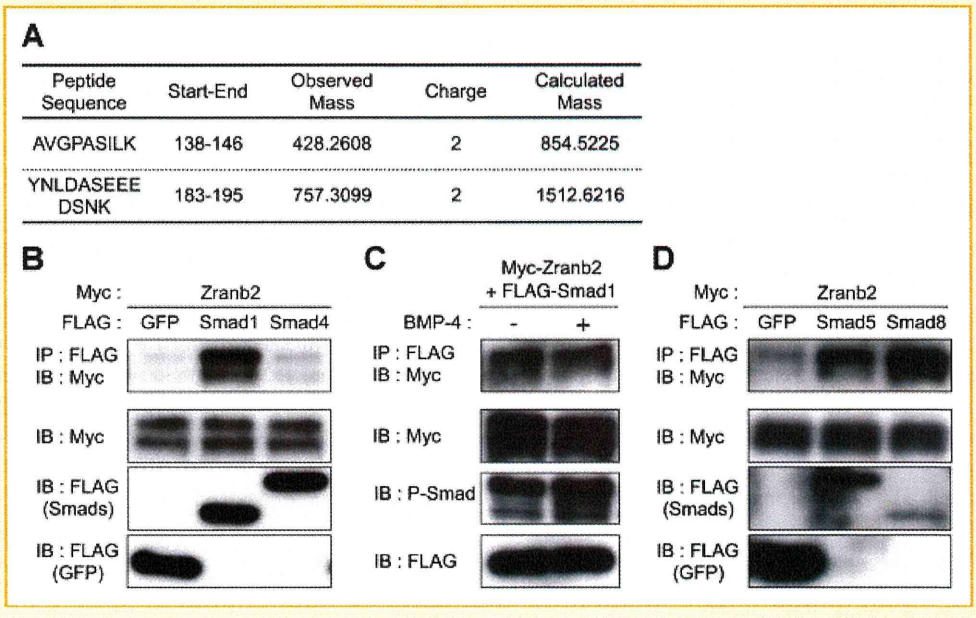

Fig. 1. Zranb2 interacts with Smads. A: Identification of ZRANB2 by LC-MS/MS analysis. The amino acid sequence assigned to each peptide and its position in the ZRANB2 sequence. Also indicates observed mass and charge of the peptide ion together with calculated mass. B, D: HEK293T cells were co-transfected with Myc-tagged Zranb2 and Flag-tagged Smad1 or Smad4 (B), Flag-tagged Smad5 or Smad8 (D) constructs. Whole cell lysates were immunoprecipitated (IP) with an α-FLAG antibody and immunoblotted with an α-Myc antibody. C: HEK293T cells were transfected with Myc-Zranb2 and Flag-Smad1 and treated for 1 h with or without 100 ng/ml BMP-4. Whole cell lysates were IP with an α-FLAG antibody and immunoblotted with an α-Myc antibody.

and *Osterix* mRNA expression were measured as typical markers of the osteoblastic differentiation that is induced by BMP activity. The overexpression of Zranb2 suppressed the ALP activity and osterix mRNA, which were induced by the transient transfection of constitutively active BMPR-IA, BMPR-IA(Q233D), and Smad1 (Fig. 2A,B). The overexpression of Zranb2 also suppressed Id1WT4F luciferase reporter activity that was driven by the BRE in the *Id1* gene following BMP-4 stimulation (Fig. 2C). We observed that Zranb2 exhibited similar suppression profiles on the BMP activity in both osteoblastic MC3T3-E1 cells and primary osteoblasts (data not shown). The injection of synthetic Zranb2 mRNA into *Danio rerio* (zebrafish) embryos caused approximately 4.4% dorsalized embryos, indicating that Zranb2 has a weak BMP-inhibitory effect in developing zebrafish (Fig. 2D,E). This result was surprising since we likely expect approximately more than 50% phenotypic consequences when target genes are mutated in zebrafish [Nakamura et al., 2007]. These results suggest that Zranb2 acts as a suppressor of BMP activity in mammalian cells and in *Danio rerio* embryos.

THE SR DOMAIN OF ZRANB2 IS ESSENTIAL FOR THE INHIBITION OF BMP SIGNALING

The primary sequence of Zranb2 predicts several structurally distinct domains: Two zinc-fingers (ZFs), a glutamic acid (Glu)-rich domain, and a serine and arginine-rich (SR) domain. To identify the domain of Zranb2 that is crucial for BMP inhibition, we generated a series of deletion mutants of Myc-Zranb2 lacking the ZFs and/or the Glu and/or SR domains (Fig. 3A). Our immunohistochemical analysis using an anti-Myc antibody indicated that the ΔZF1, ΔZF, and SR mutants were localized in the nucleus and suppressed the BMP activity similar to the wild-type Zranb2 (Fig. 3B,C). However, the ΔSR mutant was mainly localized in the cytoplasm and showed a slight enhancement, rather than an inhibition, of BMP signaling (Fig. 3B,C). We further examined the interactions of these mutants with Smad1 in a co-immunoprecipitation assay. Unexpectedly, the ΔSR mutant bound to Smad1 despite the loss of the BMP inhibition (Fig. 3D). In contrast, the SR mutant did not interact with Smad1 but suppressed BMP activity (Fig. 3D). These results suggest that the Glu and SR domains may be required for Smad interactions and BMP inhibition, respectively (see the Discussion section). In addition, we demonstrated that the MH2 domain of Smad1 was a Zranb2-interacting domain (Fig. 3E).

ZRANB2 SUPPRESSES THE TRANSCRIPTIONAL ACTIVITY OF SMADS WITHOUT INHIBITING THEIR DNA-BINDING ACTIVITY

To clarify the molecular mechanisms of Zranb2, we examined the effect of Zranb2 on the early events that are induced by BMP signaling, which include Smad phosphorylation and nuclear localization. Equivalent levels of phosphorylated Smad1/5/8 that were induced by BMPR-IA(Q233D) were detected in the presence and absence of Zranb2 (Fig. 4A). We demonstrated that phosphorylated Smad1/5/8 were localized in the nuclei in Zranb2-negative and Zranb2-overexpressing cells (Fig. 4B). Moreover, Zranb2 suppressed the BMP-specific luciferase reporter activity that was induced by the constitutively activated Smad1, Smad1(DVD), which activates the transcription of target genes, regardless of the phosphorylation status (Fig. 4C). These results suggest that the BMP receptor-mediated phosphorylation of Smad1/5/8 is not the targeted event of Zranb2-mediated suppression.

We also investigated the role of endogenous Zranb2 on the BMP activity in C2C12 cells. Transfection of two types of siRNAs against mouse Zranb2 but not scramble siRNA reduced the Zranb2 protein levels and enhanced the Id1WT4F luciferase reporter activity

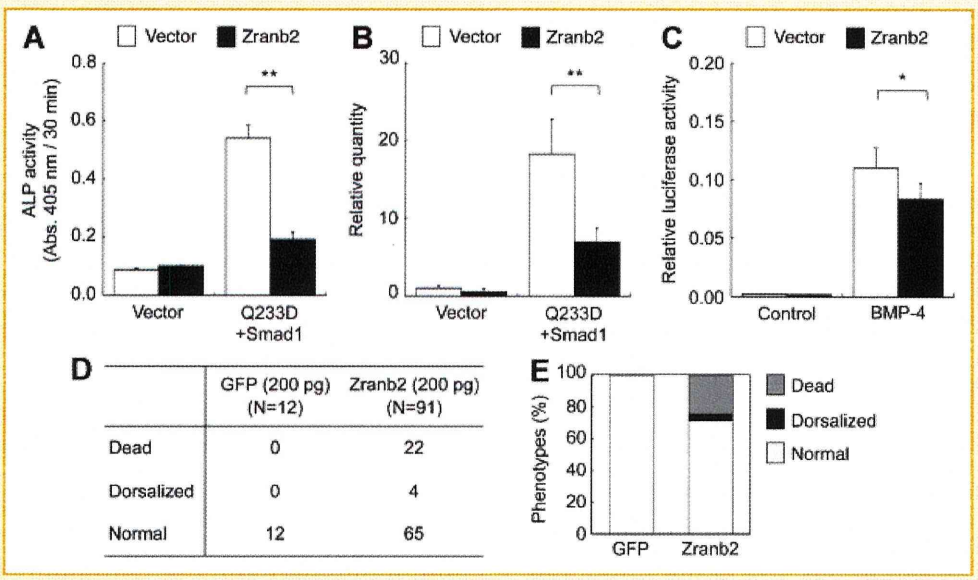

	GFP (200 pg) (N=12)	Zranb2 (200 pg) (N=91)
Dead	0	22
Dorsalized	0	4
Normal	12	65

Fig. 2. Zranb2 inhibits BMP activity. A, B: ALP activity (A) or *Osterix* mRNA expression (B) was induced by the overexpression of constitutively active BMPR-IA (Q233D) with Smad1 in the presence or absence of Zranb2 in C2C12 cells. C: IdWT4F-luc activity was induced by BMP-4 (5 ng/ml) in C2C12 cells that were transfected with or without Zranb2. D, E: Zranb2 induces weak dorsalization of the zebrafish embryo; synthetic Zranb2 mRNA (200 pg) was injected into the embryos. Results are presented as the mean ± SD ($n = 3$), $^{*}P < 0.05$ and $^{**}P < 0.01$ compared with control.

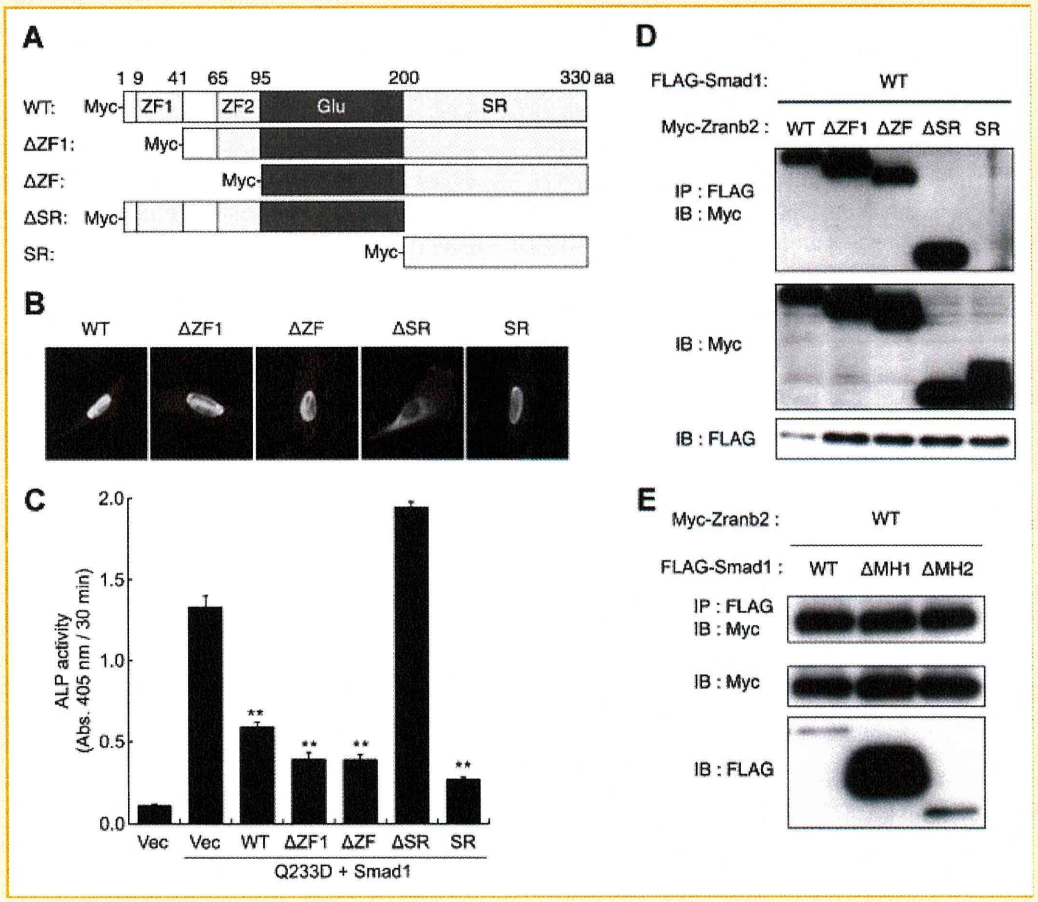

Fig. 3. The SR domain of Zranb2 is important for the inhibition of BMP activity. A: Construction of the deletion mutants of Zranb2. ZF1 and ZF2, zinc finger domains; Glu, a glutamic acid-rich domain; and SR, a serine and arginine-rich domain. B: Cellular localization of the Zranb2 mutants. C2C12 cells were transfected with one of the Zranb2 mutants followed by immunofluorescent staining with an α-Myc antibody. Original magnification, ×40. C: The SR domain suppressed the BMP activity. The ALP activity was induced by the overexpression of BMPR-IA(Q233D) and Smad1 in the presence or absence of Zranb2 in C2C12 cells. D: Analysis of the binding capacities of the Zranb2 mutants to Smad1. HEK293T cells were co-transfected with FLAG-tagged Smad1 and one of the Myc-tagged Zranb2 constructs. Whole-cell lysates were immunoprecipitated with an α-FLAG antibody and immunoblotted with an α-Myc antibody. E: The analysis of the binding capacities of the MH1 and MH2 domains of Smad1 to Zranb2. HEK293T cells were co-transfected with Myc-tagged Zranb2 and Flag-tagged Smad1(ΔMH1) or Smad1(ΔMH2). Whole cell lysates were immunoprecipitated with an α-FLAG antibody and immunoblotted with an α-Myc antibody. Results are presented as the mean ± SD (n = 3), $^{*}P < 0.05$ and $^{**}P < 0.01$ compared with control.

(Fig. 4D,E). These results suggest that Zranb2 physiologically suppresses BMP activity. However, equivalent amounts of phosphorylated Smad1/5/8 were bound to the BRE in a DNA-precipitation assay in the presence and absence of Zranb2 siRNAs. These results suggest that Zranb2 does not block the DNA-binding capacity of Smads (Fig. 4D). In addition, Zranb2 itself was not found to interact with the BRE (Fig. 4D).

DISCUSSION

In the present study, we identified Zranb2 as a novel inhibitor of BMP activity via interactions with BMP-specific Smads. Zranb2 suppressed the BMP activity in mammalian cells *in vitro* and zebrafish embryos *in vivo*. These results suggest that Zranb2 may act as an inhibitor of BMP activity in vertebrates. This is the first report demonstrating interactions between Zranb2 and BMP signaling.

Zranb2 is an SR domain-containing nuclear protein that is ubiquitously expressed in various tissues and is conserved from nematodes to mammals [Karginova et al., 1997; Mangs and Morris, 2008]. The SR proteins are splicing factors that contain a C-terminal SR domain and an N-terminal RNA recognition ZF motif [Shen and Green, 2006]. Zranb2 recognizes RNA *via* its N-terminal ZF motifs and regulates alternative splicing in a reconstituted model *in vitro* [Loughlin et al., 2009]. However, our deletion study showed that the ZF motifs were not essential for BMP inhibition or Smad1 binding. These results suggest that the alternative splicing of RNA may not be involved in Zranb2-mediated inhibition of BMP activity. In contrast, the SR domain of Zranb2 was essential for the nuclear localization and the inhibition of BMP activity. However, this SR domain did not interact with Smad1. The Glu-rich domain may be involved in interactions with the Smad1 MH2 domain. Although ZRANB1 and ZRANB3 share conserved ZF motifs with ZRNAB2, their amino acid sequences do not show a significant similarity with the Glu-rich

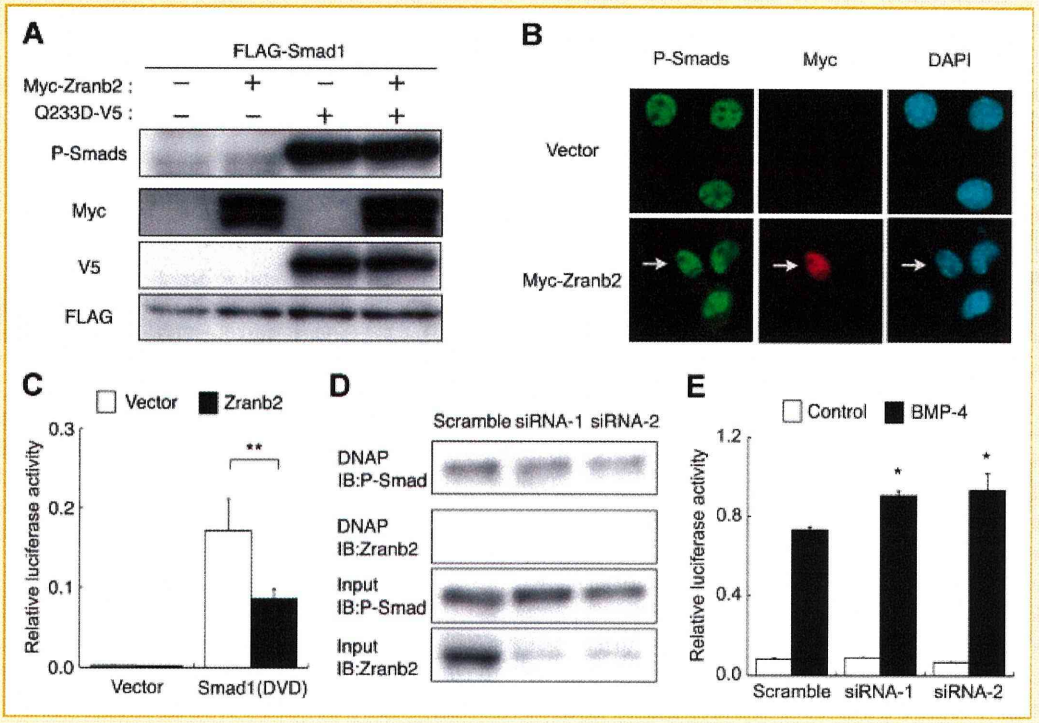

Fig. 4. Zranb2 inhibits the transcriptional activity of Smads without suppressing their DNA-binding capacity. A: Western blot analysis. C2C12 cells were co-transfected with FLAG-tagged Smad1 with or without Myc-tagged Zranb2 and V5-tagged BMPR-IA(Q233D). Whole cell lysates were immunoblotted with α-phospho-Smad1/5/8, α-FLAG, α-Myc, or α-V5 antibodies. B: C2C12 cells were transfected with Myc-tagged Zranb2 or empty vector and treated for 1 h with BMP-4 (100 ng/ml) and stained with α-phospho-Smad1/5/8 or α-Myc antibodies. Original magnification, ×40. C: Zranb2 inhibited the BMP-specific IdWT4F-luc activity that was induced by the constitutively activated Smad1, Smad1DVD. D, E: Effects of Zranb2 siRNA knockdown on the BMP activity and DNA binding of Smads. C2C12 cells were transfected with Zranb2 siRNA or scrambled siRNA. D: Nuclear extracts were affinity precipitated using the BRE and immunoblotted with α-phospho-Smad1/5/8 or α-Zranb2 antibodies. E: BMP-specific luciferase activity was induced by BMP-4. Results are presented as the mean ± SD (n = 3), $^{*}P < 0.05$ and $^{**}P < 0.01$ compared with control.

domain, SR domain, or other regions of ZRANB2 [Evans et al., 2001; Wiemann et al., 2001]. The Glu-rich and SR domains are important for the Zranb2-mediated inhibition of BMP signaling. Therefore, we hypothesized that the inhibition of BMP signaling may be unique to Zranb2 among these ZF motif-containing proteins.

Zranb2 inhibited the BMP-induced osteoblastic differentiation of the C2C12 cells and the BMP-specific luciferase reporter activity that was driven by the BRE in the *Id1* gene. However, Zranb2 did not affect the phosphorylation levels or nuclear localization of the Smads. Moreover, the DNA-binding capacity of Smads in response to BMP stimulation was not changed by the presence or absence of Zranb2, suggesting that another mechanism is involved in Zranb2-mediated inhibition. According to our results, Zranb2 interacts with the Smad1 MH2 domain, which is important for interactions with other co-activators and co-repressors, such as Smad4, p300/CBP, c-Ski, and YY1. A previous study has reported that Zranb2 co-localizes with p300 and YY1 in the nucleus [Adams et al., 2001]. Thus, it may be possible that Zranb2 outcompetes a co-activator that is essential for the transcription of target genes or recruits a co-repressor to the Smad-DNA complex on the BRE. We showed that Zranb2 was not detected on the BRE in a DNAP assay. This result supports the possibility of competition between Zranb2 and co-activators. Further studies are needed to identify and elucidate the detailed molecular mechanisms, including the critical target molecules of Zranb2 that mediate Zranb2-dependent BMP inhibition.

In conclusion, Zranb2 is a novel BMP suppressor that forms a complex with Smads in the nucleus. Our findings provide new insight into the molecular mechanisms of BMP signaling.

MATERIAL AND METHODS

Immunopurification and mass spectrometry. The FLAG-tagged Smad1 plasmid that is described below was transfected into HEK293T cells. The cytosolic extraction and immunoprecipitation procedures were performed as previously described [Komatsu et al., 2004]. The eluates from the immunoprecipitates were analyzed using nanoscale LC-MS/MS system as described previously [Natsume et al., 2002].

Plasmid constructs. Plasmids encoding the wild-type Smads, constitutively active BMPR-IA(Q233D), constitutively active Smad1(DVD), and IdWT4F-luc have been previously described [Nojima et al., 2010], [Fukuda et al., 2008]. The wild-type and mutated mouse Zranb2 (Accession number NM_017381) derivatives were obtained using standard RT-PCR techniques with PrimeStar HS DNA polymerase (TaKaRa, Shiga, Japan) and cloned into a pcDEF3 expression vector [Goldman et al., 1996]. All of the final constructs were confirmed by sequencing.

Cell culture, transfection, ALP assay, and the luciferase reporter assay. HEK293T human kidney cells, C2C12 mouse myoblasts, C3H10T1/2 mouse fibroblasts, and MC3T3-E1 mouse osteoblasts were maintained as previously described [Kokabu et al., 2011; Ohte et al., 2011]. The cells were transfected with the indicated plasmids using Lipofectamine 2000 (Invitrogen, Carlsbad, CA) according to the manufacturer's instructions. The ALP activity was measured as a marker of osteoblast differentiation as previously described [Kodaira et al., 2006]. The luciferase reporter assay was performed using IdWT4F-luc and phRL-SV40 (Promega, Madison, WI) with the Dual-Glo Luciferase Assay system (Promega) as previously described [Katagiri et al., 2002].

Immunohistochemistry, western blot, and immunoprecipitation. The following antibodies were used for the immunohistochemistry, immunoprecipitation, and western blot analysis: α-FLAG (clone M2, Sigma, St Louis, MO), polyclonal α-Myc (Medical & Biological Laboratories, Nagoya, Japan), α-V5 (clone V5005, Nacalai Tesque, Kyoto, Japan), polyclonal α-phosphorylated Smad1/5/8 (Cell Signaling Technology, Beverly, MA), polyclonal α-ZNF265(Zranb2) (E-16, Santa Cruz Biotechnology, Heidelberg, Germany), and α-MHC (clone MF-20, Developmental Studies Hybridoma Bank, Iowa City, IA). For the immunohistochemical analysis, the target proteins were visualized using the Alexa488- or Alexa594-conjugated secondary antibodies (Invitrogen). The western blot analysis was performed as previously described [Fukuda et al., 2009]. The target proteins were immunoprecipitated for 3 h at 4°C using M2-agarose beads (Sigma).

Injection of synthetic RNA into zebrafish embryos. The full-length Zranb2 sequence was cloned into the pCS2+ expression vector, and RNA was synthesized from NotI-digested pCS2+ plasmids using the SP6 mMessage mMachine kit (Ambion, Austin, TX). Phenol red (0.1%) was added to the RNA solution as a tracer, and the RNA (200 pg) was injected into 1–2 cell-stage embryos. Following the injection, the embryos were cultured in aquatic system water and imaged as previously described [Nakamura et al., 2007].

DNA affinity precipitation. The DNA affinity precipitation was performed as previously described, with some modifications [Suzuki et al., 1993]. Nuclear extracts from the C2C12 cells were prepared using the ProteoJET cytoplasmic and nuclear protein extraction kit (Fermentas, Glen Burnie, MD). The biotinylated DNA probes were prepared using PCR with biotin-conjugated primers. The biotinylated DNA probe (1 μg) and nuclear extracts (100 μg of protein) were incubated for 30 min on ice in a volume (500 μl) of a solution containing 20 mM HEPES-KOH (pH 7.9), 80 mM KCl, 1 mM $MgCl_2$, 0.2 mM EDTA, 0.5 mM DTT, 5%(v/v) glycerol, protease inhibitor cocktail (Roche Diagnostics GmbH, Mannheim, Germany), and phosphatase inhibitor (Nacalai Tesque). Dynabeads M-280 streptavidin (Invitrogen) were added and mixed by rotation for 1 h at 4°C. The collected proteins were subjected to western blot analysis as described above.

Reverse transcriptase PCR and real-time PCR analysis. Total RNA was isolated using TRIzol (Invitrogen) and reverse-transcribed into cDNA using Superscript III (Invitrogen). The cDNA was amplified using PCR with specific primers for *Osterix*, *Alp*, *Osteocalcin*, and *Atp5f1* (TaKaRa). *Atp5f1* was used as control. SYBR green-based real-time PCR was performed in a 96-well plate format SYBR Premix Ex Taq (TaKaRa) and a Thermal Cycler Dice Real-time system TP800 (TaKaRa).

Statistical analysis. An unpaired Student's *t*-test was used for the comparisons. The data are expressed as the mean ± SD, and the statistical significance is indicated as $^{*}P < 0.05$ and $^{**}P < 0.01$.

ACKNOWLEDGMENTS

The authors are grateful to Dr. J. A. Langer for kindly providing pcDEF3. This work was supported in part by Health and Labour Sciences Research Grants for Research on Measures for Intractable Research from the Ministry of Health, Labour and Welfare of Japan, grants-in-aid from the Ministry of Education, Culture, Sports, Science, and Technology of Japan, a grant-in-aid from the Takeda Science Foundation, and a grant-in-aid for the "Support Project of Strategic Research Center in Private Universities" from the Ministry of Education, Culture, Sports, Science and Technology (MEXT) to Saitama Medical University Research Center for Genomic Medicine.

REFERENCES

Adams DJ, van der Weyden L, Mayeda A, Stamm S, Morris BJ, Rasko JE. 2001. ZNF265–a novel spliceosomal protein able to induce alternative splicing. J Cell Biol 154:25–32.

Akiyoshi S, Inoue H, Hanai J, Kusanagi K, Nemoto N, Miyazono K, Kawabata M. 1999. c-Ski acts as a transcriptional co-repressor in transforming growth factor-beta signaling through interaction with smads. J Biol Chem 274: 35269–35277.

Evans PC, Taylor ER, Coadwell J, Heyninck K, Beyaert R, Kilshaw PJ. 2001. Isolation and characterization of two novel A20-like proteins. Biochem J 357:617–623.

Feng XH, Zhang Y, Wu RY, Derynck R. 1998. The tumor suppressor Smad4/DPC4 and transcriptional adaptor CBP/p300 are coactivators for smad3 in TGF-beta-induced transcriptional activation. Genes Dev 12:2153–2163.

Fukuda T, Kanomata K, Nojima J, Kokabu S, Akita M, Ikebuchi K, Jimi E, Komori T, Maruki Y, Matsuoka M, Miyazono K, Nakayama K, Nanba A, Tomoda H, Okazaki Y, Ohtake A, Oda H, Owan I, Yoda T, Haga N, Furuya H, Katagiri T. 2008. A unique mutation of ALK2, G356D, found in a patient with fibrodysplasia ossificans progressiva is a moderately activated BMP type I receptor. Biochem Biophys Res Commun 377:905–909.

Fukuda T, Kohda M, Kanomata K, Nojima J, Nakamura A, Kamizono J, Noguchi Y, Iwakiri K, Kondo T, Kurose J, Endo KI, Awakura T, Fukushi J, Nakashima Y, Chiyonobu T, Kawara A, Nishida Y, Wada I, Akita M, Komori T, Nakayama K, Nanba A, Maruki Y, Yoda T, Tomoda H, Yu PB, Shore EM, Kaplan FS, Miyazono K, Matsuoka M, Ikebuchi K, Akira O, Hiromi O, Eijiro J, Ichiro O, Yasushi O, Takenobu K. 2009. Constitutively activated ALK2 and increased smad1/5 cooperatively induce BMP signaling in fibrodysplasia ossificans progressiva. J Biol Chem 284:7149–7156.

Goldman LA, Cutrone EC, Kotenko SV, Krause CD, Langer JA. 1996. Modifications of vectors pEF-BOS, p cDNA1 and pcDNA3 result in improved convenience and expression. Biotechniques 21:1013–1015.

Itoh S, Ericsson J, Nishikawa J, Heldin CH, ten Dijke P. 2000. The transcriptional co-activator P/CAF potentiates TGF-beta/Smad signaling. Nucleic Acids Res 28:4291–4298.

Karginova EA, Pentz ES, Kazakova IG, Norwood VF, Carey RM, Gomez RA. 1997. Zis: A developmentally regulated gene expressed in juxtaglomerular cells. Am J Physiol 273:F731–F738.

Katagiri T, Imada M, Yanai T, Suda T, Takahashi N, Kamijo R. 2002. Identification of a BMP-responsive element in Id1, the gene for inhibition of myogenesis Genes Cells 7:949–960.